Temperature-driven phase transitions from first principles including all relevant excitations: The fcc-to-bcc transition in Ca

B. Grabowski, P. Söderlind, T. Hickel, and J. Neugebauer

Temperature-driven phase transitions from first principles including all relevant excitations: The fcc to bcc transition in Ca

B. Grabowski and P. Söderlind

Lawrence Livermore National Laboratory, Livermore, California 94550, USA

T. Hickel and J. Neugebauer

Max-Planck-Institut für Eisenforschung GmbH, D-40237, Düsseldorf, Germany

(Dated: November 30, 2011)

The temperature-driven fcc to bcc phase transition in calcium is examined by a fully *ab initio* based integrated technique including all relevant finite temperature excitation mechanisms. The approach is based on density-functional-theory calculations with a controlled numerical stability of below 0.5 meV/atom for the electronic, quasiharmonic, and structural excitations, and better than 1 meV/atom for the explicitly anharmonic contribution. The latter is achieved by successfully utilizing the recently developed hierarchical *upsampled thermodynamic integration using Langevin dynamics* method. This approach gives direct access to a numerically highly precise volume and temperature dependent free energy surface and derived properties. It enables us to assign the remaining deviations from experiment to inherent errors of the presently available exchange-correlation-functionals. Performing the full analysis with both of the conventional functionals, LDA and GGA, we demonstrate that – when considered on an absolute scale – thermodynamic properties are dictated by a strikingly similar free energy vs. volume curve. Further we show that, despite an error in the $T=0\,\mathrm{K}$ energy difference between the two phases (≈ 6 meV in the present case), an excellent agreement of the temperature dependence of the Gibbs energy difference with experimentally derived data is possible. This allows, for instance, to unveil unreliable and possibly erroneous experimental input used in popular thermodynamic databases as we explicitly demonstrate for the isobaric heat capacity of calcium.

PACS numbers:

I. MOTIVATION

For roughly two decades, *ab initio* based methods for pressure-driven phase transitions have been successfully applied to various materials. Prominent examples include calcium,[1] iron,[2] and even much more complex materials such as actinides.[3] In contrast, an accurate and complete *ab initio* description of temperature-driven transitions is still in its infancy even for simple elementary metals. Corresponding studies are rare[4,5] and a reliable extension to complex materials will only be feasible upon major advances in the field.

The main reason for the difficulty of dealing with temperature-induced phenomena is twofold: 1) The relevant energy scales differ typically by at least one order of magnitude. While pressure dictated transitions are often determined by energy differences of a few dozen meV/atom, a temperature description generally relies on (free) energy differences of a few meV/atom. Obtaining such accuracy and stability is a demanding and challenging *ab initio* task. 2) While pressure-induced transitions can usually be reasonably resolved by considering solely the $T=0\,\mathrm{K}$ contribution, the situation completely changes for temperature-induced transitions. The reason is that various excitations become available and these will be eventually the driving force for the transition. An accurate *ab initio* description of such finite temperature excitations is, however, a challenging task due to the large phase space which needs to be sampled.

Calcium is in this respect a prototypical example. Its temperature-pressure phase diagram contains interesting and technologically important phases. Much interest in calcium is due to its remarkable superconducting properties.[6] As a consequence pressure-induced transitions have been intensively studied with *ab initio* methods. Moreover, calcium shows also a temperature-induced transition from fcc to bcc. This issue has been addressed using *ab initio* methods,[4] albeit including only non-interacting phonon excitations (quasiharmonic approximation) to the free energy. This contribution dominates the free energy at finite temperatures in absolute terms. However, small energy differences can be crucial for temperature-driven transitions and a detailed balance of higher order contributions, such as anharmonicity, must be explored.

A major goal of the present study is to shed light on the role of all relevant finite temperature contributions to the fcc to bcc phase transition in calcium (Sec. IV B). The study is performed utilizing a fully self consistent and integrated *ab initio* approach (Sec. II) firmly founded on density-functional-theory[7] (DFT). We consider electronic, quasiharmonic, anharmonic, and vacancy excitations (Secs. III A to III E) with a special focus on extreme numerical precision. For the standard contributions we guarantee a convergency of better than 0.5 meV/atom, while anharmonicity is captured below 1 meV/atom. This accuracy allows to correlate remaining discrepancies between our calculation and experiment to DFT errors related to the unavoidable approximation in the exchange

correlation (xc) functional. In particular we are able to reveal a free energy vs. volume curve that is – to a good approximation – independent of the used xc functional if considered on an absolute scale (Secs. IV C and IV D).

Besides a detailed investigation of the phase transition, we provide a comparison with experiment for various derived thermodynamic properties (Secs. IV D and IV E). For that purpose, we compile a large set of available experimental data. On the theoretical side, we compute the full volume and temperature dependent Helmholtz free energy surface allowing us to extract properties at constant pressure and thus providing a sound basis for an unbiased comparison. Based on this approach we are able to resolve a systematic discrepancy between two sets of experimental data for the isobaric heat capacity of calcium (Sec. IV E).

II. GENERAL METHODOLOGY

As indicated above the central quantity in this study is the Helmholtz free energy surface $F(V, T)$ as a function of volume V and temperature T. For each of the considered phases, fcc and bcc, there is one such surface. The Helmholtz free energy is a theoretically conveniently accessible thermodynamic potential and provides access to all experimental thermodynamic properties. Experiments are typically performed at constant pressure P and we therefore need to perform a Legendre transformation to the Gibbs energy $G(P, T) = F(V, T) + PV$. We will focus on the following derived quantities at ambient pressure: Gibbs energy difference between bcc and fcc, volume expansion $V(T)$, the isothermal bulk modulus $B_T(T)$, and in particular the isobaric heat capacity $C_P(T)$:[8]

$$V(T) = \left[\frac{\partial G(P, T)}{\partial P} \right]_T, \tag{1}$$

$$B_T(T) = \frac{1}{\kappa} \quad \text{with} \quad \kappa = -\frac{1}{V(T)} \left[\frac{\partial^2 G(P, T)}{\partial P^2} \right]_T, \tag{2}$$

$$C_P(T) = -T \left[\frac{\partial^2 G(P, T)}{\partial T^2} \right]_P. \tag{3}$$

To allow a convenient comparison with experiment we convert the volume expansion into a linear expansion $\epsilon(T)$ and a linear expansion coefficient $\alpha(T)$ according to

$$\epsilon(T) = \frac{L(T) - L^{\text{ref}}}{L^{\text{ref}}}, \quad \alpha(T) = \frac{1}{L(T)} \frac{\partial L(T)}{\partial T}, \tag{4}$$

where $L(T) = [V(T)]^{1/3}$ and $L^{\text{ref}} = [V_{0\text{K}}^{\text{fcc}}]^{1/3}$, with $V_{0\text{K}}^{\text{fcc}}$ the equilibrium volume of the fcc phase at $T = 0$ K (and given pressure P). Note that $V(T)$ is here assumed to be given per atom in order to guarantee consistency between fcc and bcc and that the reference volume corresponds always to the fcc phase. The latter is in particular true

even when we consider the linear expansion of the high temperature bcc phase.

The surface $F(V, T)$ for each phase is completely obtained within DFT methodology. While in principle exact, a practical DFT implementation relies on an approximation of the electron exchange and correlation. The two most commonly used assumptions are the local density approximation (LDA) and the generalized gradient approximation (GGA). Our philosophy is to calculate all properties using both approximations, an approach found to be very useful for estimating intrinsic error bars.[9]

Focussing first on the perfect crystal [vacancies are added in Eq. (6)], we separate the free energy into the following terms

$$F = E_{0\text{K}} + \widetilde{F}^{\text{el}} + F^{\text{qh}} + F^{\text{ah}}, \tag{5}$$

with $E_{0\text{K}}$ being volume dependent and the other terms both volume and temperature dependent. In Eq. (5), $E_{0\text{K}}$ is the zero-temperature total electronic energy, $\widetilde{F}^{\text{el}}$ the electronic free energy (the tilde reminding us that $E_{0\text{K}}$ is not included), F^{qh} the quasiharmonic free energy, and F^{ah} the explicitly anharmonic free energy.

The total electronic energy $E_{0\text{K}}$ is calculated within the framework of "standard" DFT,[7] while $\widetilde{F}^{\text{el}}$ requires the finite temperature extension of DFT by Mermin.[10] The quasiharmonic approximation used to obtain F^{qh} is a general (not necessarily requiring DFT) and well established approach (see, e.g., Ref. [11]) based on non-interacting but volume dependent phonons. It has been applied in the context of DFT since the late 1980's (e.g., Ref. [12]). The biggest challenge is related to the computation of the explicitly anharmonic part F^{ah}, which involves the interaction of phonons with themselves. Due to demanding computations, DFT based investigations of anharmonicity have been put forward only recently with Ref. [13] being one of the pioneering studies.

In the present work, we utilize the recently developed *upsampled thermodynamic integration using Langevin dynamics* (UP-TILD) method[14] to efficiently calculate F^{ah}. The UP-TILD method is a multi-step approach with a Langevin dynamics based thermodynamic integration at its core. It provides a high accuracy in F^{ah} within only a few 100 molecular dynamics steps at the highest convergence level. The approach relies on the observation that certain convergence parameters such as k-point sampling and energy cutoff are mainly needed to converge the kinetic electronic energy, while the charge density is well described already at significantly reduced parameters. Thus, increasing convergence gives rise to a substantial volume dependent shift in the energies, but affects the forces and thus the shape of the potential energy surface only little. With this knowledge, one can design a hierarchical scheme with varying convergence parameters optimized for highest efficiency.[14]

A surface according to Eq. (5) is calculated for a perfect fcc and bcc crystal as well as for crystals containing a single point defect. This allows to fully include the effect

of thermodynamically excited point defects on thermodynamic properties within the non-interacting regime. We specifically consider vacancies since other point defects such as interstitials are thermodynamically irrelevant due to high formation energies.[15] In particular we compute the complete temperature dependence of the Gibbs energy of vacancy formation including all of the above mentioned excitation mechanisms (electronic, quasiharmonic, and anharmonic). Inclusion of the anharmonic term has been found to be important for an accurate determination of the entropy of formation.[16]

The final Gibbs energy surface $G(P,T)$ as a function of pressure P and temperature T is obtained from:[8]

$$G(P,T) = F^{\mathrm{p}}(V_P, T) + PV_P - k_{\mathrm{B}}T\, c^{\mathrm{eq}}(P,T). \quad (6)$$

Here, the Helmholtz free energy of the perfect crystal F^{p} is calculated according to Eq. (5) and at a volume V_P which is consistently adjusted to correspond to the given pressure P. The latter is volume and temperature dependent and related to the free energy surface by $P = -\partial F^{\mathrm{p}}/\partial V_P$ and we stress that we perform the derivative on the full free energy surface including all excitations. This gives us not only self-consistent access to the thermal part of the pressure term arising from ionic vibrations, but also to the contribution of the other excitations. Further in Eq. (6), k_{B} is the Boltzmann constant and c^{eq} is the equilibrium vacancy concentration obtained from

$$c^{\mathrm{eq}}(P,T) = \exp[-G^{\mathrm{f}}(P,T)/(k_{\mathrm{B}}T)], \quad (7)$$

with G^{f} denoting the fully pressure and temperature dependent Gibbs energy of vacancy formation (Sec. III E).

III. METHODOLOGICAL DETAILS

The calculations are performed within the projector augmented wave (PAW) method[17] as implemented in the VASP software package[18,19] in combination with the provided PAW potentials.[20] In particular, we employ a calcium PAW potential treating the 8 highest electrons as valence electrons ($3p^6 4s^2$) for both LDA and GGA calculations. Convergence parameters are in general adjusted to give errors of below 0.5 meV/atom for $E_{0\mathrm{K}}$, $\widetilde{F}^{\mathrm{el}}$, and F^{qh} and below 1 meV/atom for F^{ah} at all temperatures and volumes. The convergence parameters are explicitly given in the following subsections.

The accuracy of the PAW potential is carefully evaluated for the $E_{0\mathrm{K}}$ and $\widetilde{F}^{\mathrm{el}}$ contributions using two distinct all-electron approaches: the full-potential (linearized) augmented plane wave (FLAPW) + local orbital method[21] as implemented in WIEN2K[22] and a full potential linear muffin-tin orbitals (FPLMTO) method.[23] Sections III A and III B give the details of the all-electron calculations and Tab. III and Fig. 7c show the results.

As for the xc electron energy and potential functionals we use the LDA as well as the GGA approximation.

For LDA we apply the scheme of Ceperley-Alder[24] as parametrized by Perdew and Zunger.[25] For GGA we use the Perdew-Burke-Ernzerhof[26] (PBE) parametrization.

A. $T=0\,\mathrm{K}$ energy

For our high accuracy purposes, it turns out to be necessary to use a careful procedure for obtaining the $T=0\,\mathrm{K}$ electronic binding energy $E_{0\mathrm{K}}$ [Eq. (5)]. This contribution is practically not directly accessible, since at $T=0\,\mathrm{K}$ the Fermi distribution corresponds to a step function resulting in high numerical problems. We find that a simple extrapolation scheme for $E_{0\mathrm{K}}$ based on the ideal entropy can result in an error of several meV/atom if used in combination with the Fermi broadening. The (first order) Methfessel-Paxton scheme,[27] which introduces artificial (even negative) occupancies at the expense of an unphysical electronic free energy, is more suited for the purpose of giving an accurate extrapolation for $E_{0\mathrm{K}}$. We ensure, however, that upon a careful (small broadening with sufficient k-points) extrapolation we arrive at the same and exact $E_{0\mathrm{K}}$ also with the Fermi-Dirac scheme.

To parametrize the $T=0\,\mathrm{K}$ energy-volume dependence we use the Vinet equation of state[28] (volume range $\approx -10\%\ldots 12\%$ around equilibrium). This equation of state has been found to describe theoretical and experimental curves of various materials most accurately.[29] We work with >1650 k-points in the irreducible Brillouin zone and with a plane wave cutoff of 300 eV when calculating $E_{0\mathrm{K}}$ for both functionals and both phases. These values guarantee an energy convergency of well below 0.1 meV/atom in the bcc-fcc energy difference in the full volume range giving an excellent and unbiased starting point for the free energy calculations.

For the FLAPW calculations we use constant muffin-tin sphere radii of $R_{\mathrm{MT}} = 2.8$ Bohr radius for both GGA and LDA. The product of the muffin-tin sphere radius and the maximum reciprocal space vector, $R_{\mathrm{MT}}k_{\mathrm{max}}$, is set to 12. The k-point sampling is equivalent to that in the PAW calculations. The maximum l value for the waves inside the muffin-tin spheres and the largest reciprocal vector $\vec{G}$ in the charge Fourier expansion are set to $l_{\mathrm{max}} = 12$ and $G_{\mathrm{max}} = 18$ (Bohr radius)$^{-1}$, respectively. Relativistic effects are fully included within the muffin-tin spheres and using the scalar relativistic approximation in the valence region.

The details of the FPLMTO calculations are similar to the ones for the FLAPW method. Instead of using a fixed muffin-tin sphere radius, R_{MT}, the latter is scaled with the atomic sphere radius, R_{AS}, so that $R_{\mathrm{MT}}/R_{\mathrm{AS}} = 0.86$. The results are, however, insensitive to the scaling factor. The basis functions include $3s$ and $3p$ semi-core states in addition to the $spdf$ valence states. Each function has three energy tails for a total of 18 basis functions in this triple-basis set up. The calculations are carefully checked for convergence with respect to k-points and the expansion of the basis functions (in the interstitial) in

Fourier series. The effect of spin-orbit coupling is found to be negligible.

B. Electronic excitations

The exact approach to obtain the T dependent part of the electronic free energy $\widetilde{F}^{\mathrm{el}}$ reads

$$\widetilde{F}^{\mathrm{el}}(V,T) = F^{\mathrm{el}}(V,T) - E_{0\mathrm{K}}(V), \qquad (8)$$

where F^{el} is the total electronic free energy including the $T=0\,\mathrm{K}$ binding energy $E_{0\mathrm{K}}$. Within finite temperature DFT, $F^{\mathrm{el}}(T)$ is the fundamental quantity derived directly from a corresponding calculation with T determining the Fermi broadening, while $E_{0\mathrm{K}}$ needs to be separately obtained by careful extrapolation as discussed in the preceding section.

We evaluate the performance of the following common approximation to Eq. (8)

$$\widetilde{F}^{\mathrm{el}}(T) \approx -\frac{1}{2}TS^{\mathrm{el}}(T), \qquad (9)$$

where S^{el} is the (ideal) electronic entropy obtained from Fermi occupation numbers $f(\epsilon)$ and the electronic density of states $N^{\mathrm{el}}(\epsilon)$ by (spin unpolarized):[30]

$$S^{\mathrm{el}}(T) = -2k_{\mathrm{B}} \int d\epsilon \ N^{\mathrm{el}}(\epsilon) \ [f \ln f + (1-f)\ln(1-f)]. \qquad (10)$$

Both N^{el} and f are explicitly temperature dependent

$$N^{\mathrm{el}} = N^{\mathrm{el}}(\epsilon, T) \quad \text{and} \quad f = f(\epsilon, T) = \frac{1}{\exp[\frac{\epsilon}{k_{\mathrm{B}}T}]+1}, \qquad (11)$$

with the temperature dependence of N^{el} being fully captured by a self consistent finite temperature DFT calculation. Note that Eq. (9) is directly related to the simple extrapolation scheme for $E_{0\mathrm{K}}$ referred to in the previous section, since from Eqs. (8) and (9) we directly obtain $E_{0\mathrm{K}} = F^{\mathrm{el}} - \widetilde{F}^{\mathrm{el}}$.

Approximation Eq. (9) turns out to be insufficient for our high accuracy purposes, since it can introduce an error of a few meV/atom at higher temperatures. An example for the performance of this approximation is given in Fig. 7d. To achieve full accuracy in $\widetilde{F}^{\mathrm{el}}$ we therefore base all our calculations on the exact formula Eq. (8).

Despite the fact that a calculation of the $\widetilde{F}^{\mathrm{el}}(V,T)$ surface is nowadays a computationally straightforward task, the determination of derivative quantities such as heat capacities or expansion coefficients requires a well defined parametrization of $\widetilde{F}^{\mathrm{el}}(V,T)$. The reason is that a numerical differentiation – even on a dense grid – would result in significant noise in these quantities, since they are sensitive to extremely small free energy differences. The parametrization of the volume dependence of $\widetilde{F}^{\mathrm{el}}$ is typically simple, since the $T=0\,\mathrm{K}$ binding energy $E_{0\mathrm{K}}$ (which carries a stronger dependence) has been separated

out. A polynomial ansatz is therefore well motivated and indeed we find a 2nd order polynomial sufficient to fit $\widetilde{F}^{\mathrm{el}}(V)$ with an error of ≈ 0.1 meV/atom.

For the temperature dependence a direct polynomial fit, i.e., $\widetilde{F}^{\mathrm{el}}(T) = \sum_i c_i T^i$, turns out to be reasonable. We are, however, able to devise a more physical and accurate fit, particularly for the low temperature regime. For that purpose, we utilize Eqs. (9) and (10) as given but with the electronic density of states N^{el} as the fitting quantity. In particular, at each considered volume we take N^{el} to be energy independent while expanding its temperature dependence into a polynomial

$$N^{\mathrm{el}}(V,T) = \sum_i c_i(V)T^i, \qquad (12)$$

where the c_i are used as fitting parameters. With $i = 0\ldots3$ we are able to achieve fits with an error well below 0.1 meV/atom at all temperatures and volumes. Note that with this fitting procedure we are not falling back to the accuracy of approximation Eq. (9). We are just utilizing its physical temperature dependence, while – due to the fitting procedure – being consistent with information stored in the exact formula Eq. (8).

The input to the fit is a mesh of at least 10 equidistantly spaced volumes and 10 temperatures of explicitly calculated $\widetilde{F}^{\mathrm{el}}$ points in the relevant range for each surface. The relevant range is determined by zero Kelvin, the experimental melting temperature[31] of 1115 K, and the respective equilibrium volumes at these temperatures. Further, we use >1650 k-points in the irreducible Brillouin zone and a cutoff of 150 eV leading to an error well below 0.1 meV/atom.

The FLAPW calculations for $\widetilde{F}^{\mathrm{el}}$ are performed with WIEN2K[22] and are based on the same parameters as given in the preceding section.

C. Quasiharmonic vibrations

1. Effect of electronic temperature

The (quantum mechanical) quasiharmonic free energy F^{qh} follows from volume dependent, but non-interacting phonon frequencies $\omega_q = \omega_q(V)$ by means of the standard expression[11]

$$F^{\mathrm{qh}}(T) = \frac{1}{m^3}\sum_q^{3m^3}\left\{\frac{\hbar\omega_q}{2} + k_{\mathrm{B}}T\ \ln\left[1 - \exp\left(-\frac{\hbar\omega_q}{k_{\mathrm{B}}T}\right)\right]\right\}, \qquad (13)$$

with the reduced Planck constant $\hbar$. The ω_q are lying on a dense and converged mesh in Fourier space with m^3 points (here: $m=16$) and with the index q running over these points and additionally over the three branches (unary crystal). In fact, the non-interacting ω_q are not only volume dependent but also explicitly dependent on the electronic temperature/broadening. This is

a result of the so called free energy Born-Oppenheimer approximation,[32] which is a thermodynamic extension of the standard Born-Oppenheimer approximation.[33]

The main result of the free energy Born-Oppenheimer approximation is that the ionic movement is determined by the temperature dependent electronic free energy surface $F^{el}(\{\mathbf{R}_I\}, T)$, where $\{\mathbf{R}_I\}$ denotes the set of atomic coordinates (see, e.g., Ref. [16] for details). An immediate consequence is that the dynamical matrix D, which yields upon Fourier transformation and diagonalization the frequencies ω_q, needs to be obtained from the second derivative of $F^{el}(\{\mathbf{R}_I\}, T)$, i.e., for a unary crystal of atomic mass M

$$D_{kl}(V,T) = \frac{1}{M}\left[\frac{\partial^2 F^{el}(\{\mathbf{R}_I\}, V, T)}{\partial R_k \partial R_l}\right]_{\{\mathbf{R}_I^0\}}, \qquad (14)$$

where k and l run over atoms and spatial directions and where $\{\mathbf{R}_I^0\}$ denotes the set of equilibrium positions. The dynamical matrix carries therefore an explicit temperature dependence and this dependence is transfered to the resulting phonon frequencies

$$\omega_q \quad \rightarrow \quad \omega_q(V, T^{el}), \qquad (15)$$

with the superscript making explicit that we refer here to the electronic Fermi broadening within a finite temperature DFT calculation.

In Ref. [14], the actual influence of T^{el} on phonons and the resulting quasiharmonic free energy has been investigated. Ref. [14] shows that it can be safely neglected in the case of aluminum. In contrast, in Ref. [34] it has been found that for rhodium, which has a higher density of states at the Fermi level, F^{qh} can change by a few meV/atom with varying T^{el}. Since calcium shows also a non-negligible density of states at the Fermi level (see Fig. 5c), we carefully investigated the T^{el} influence.

For that purpose, we calculate the dynamical matrix in Eq. (14) at various electronic temperatures and volumes. We include also the $T^{el}=0$ K calculation by utilizing the Methfessel-Paxton scheme.[27] It turns out that the T^{el} influence is very small in the fcc phase. Even upon changing the Fermi broadening from 0 to 1160 K ($\hat{=}0.1$ eV; close to the melting temperature) the change in the fcc phonon energies is below 0.3 meV. As a direct consequence, also the effect on the quasiharmonic free energy is small in fcc (<0.5 meV/atom). For the bcc phase, we observe the same behavior in all branches except for the low energetic $T_1[110]$ branch, which experiences phonon shifts in the range of 2 meV (Fig. 5a). Of even greater importance is the fact that the GGA phonon dispersion shows a dynamical instability in this branch at $T^{el}=0$ K, which can be lifted upon increasing T^{el}. Due to the importance of the involved physics, we postpone the corresponding discussion to Sec. IV A. At this point, we focus on the numerical consequences for the quasiharmonic free energy. The latter needs to be calculated cautiously, since an improper treatment may lead to divergent terms in Eq. (13).

We use the following procedure to avoid the instability occurring in the GGA bcc $T_1[110]$ branch. First, we fix the electronic temperature to a value of 1160 K at which the instability nearly fully disappears. Second, we choose a frequency mesh that does not resolve the remaining small instability region (Fig. 5a), but which is fully converged in any other region of the Brillouin zone. We use this choice in Eq. (13) to calculate F^{qh} thus avoiding diverging terms from the instability. This is equivalent to projecting out the long wave length limit at which the instability occurs by employing a finite size effect. The procedure is well justified and entails no inaccuracy for our purposes due to the following arguments:

1. Note first that T^{el} affects solely the $T_1[110]$ branch, while its effect is negligible on all other frequencies (Fig. 5a). The $T_1[110]$ branch corresponds, however, to a small part of the full 3D Brillouin zone and thus enters Eq. (13) only with a small weighting factor. This is demonstrated in Fig. 1a. Changing T^{el} from 800 K (close to transition temperature) to 1160 K (close to melting) affects F^{qh} by less than 0.1 meV/atom. In fact, we can go further and calculate F^{qh} at $T^{el}=0$ K by projecting out again the (now larger) instability region. Fig. 1a shows that even in this extreme case F^{qh} changes by no more than 0.5 meV/atom for the largest supercell.

2. For the frequencies on the $T_1[110]$ branch which are captured by the supercells used for the anharmonic calculations (exact frequencies) the fixed T^{el} condition is fully relaxed by utilizing the UP-TILD method (Sec. III D). This reduces further the weighting factor and confines the affected region basically to the long wave length limit.

3. Moreover, we expect the long wave length limit to be additionally stabilized by phonon-phonon interaction. An explicit evaluation of this statement is practically not feasible. We are, however, able to device a method (Sec. III F) that allows to estimate the effect due to phonon-phonon interaction also for this Brillouin zone region. We can clearly see (gray line in inset of Fig. 5a) that the phonon-phonon interaction indeed removes the instability as expected.

2. Computational details

The dynamical matrix D is calculated using the direct force constant method[35] (also referred to as the small displacement method[36,37]). A displacement of 0.03 Bohr radius is used throughout to obtain the Hellmann-Feynman forces. We ensure that this choice leads to linear forces on all atoms in the supercell. As intensively discussed in Ref. [9] an important convergence parameter when applying the force constant method in combination with the PAW method is the grid for the augmentation charges.
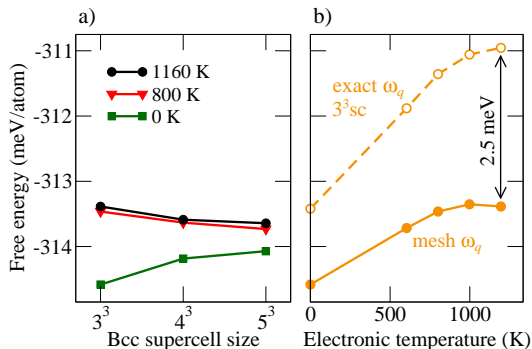
FIG. 1: (Color online) a) Supercell size convergence and b) electronic temperature (Fermi broadening) dependence of the quasiharmonic free energy of the bcc phase for the GGA-PBE functional at a lattice temperature of 716 K (experimental transition point[31]). In a) the supercell size convergence (in terms of the conventional cubic bcc unit cell) is shown for three different electronic temperatures and corresponds to frequencies on a dense Fourier mesh. In b) both curves refer to a $3\times3\times3$ bcc supercell, one is however calculated using only exact frequencies ω_q while the other is based on a dense ω_q mesh.

TABLE I: Supercell size convergence of the quasiharmonic free energy F^{qh} per atom at the experimental fcc-bcc phase-transition temperature[31] of 716 K for the GGA-PBE xc functional. A dense Fourier interpolated frequency mesh is used to calculate F^{qh}. The supercell sizes are given in terms of the cubic fcc and bcc conventional unit cells with 4 and 2 atoms, respectively.

fcc			bcc		
supercell	atoms	F^{qh}(meV)	supercell	atoms	F^{qh}(meV)
$2\times2\times2$	32	-297.9	$3\times3\times3$	54	-313.4
$3\times3\times3$	108	-298.7	$4\times4\times4$	128	-313.6
$4\times4\times4$	256	-298.6	$5\times5\times5$	250	-313.6

This is particularly crucial for elements with high electron density in the augmentation region. The chosen calcium PAW potential (8 valence electrons) has in this respect a relatively strong contribution (similar to the Ag case in Ref. [9]) and we therefore carefully test corresponding dependencies. Augmentation grids of 423×10^3 (fcc) and 864×10^3 (bcc) grid points/atom turn out to be sufficient. With these settings for the augmentation grid a plane wave cutoff of 240 eV is an accurate choice.

We take special care to satisfy the electronic k-sampling convergence, which is essential in elucidating the T^{el} dependence. The values are in the range of 23×10^3 k-points · atom. (This unit is useful when dealing with different phases or varying supercell sizes; the given value corresponds, e.g., to a $6\times6\times6$ k-mesh in a $3\times3\times3$ cubic fcc cell with 108 atoms.) We also experience that a very high energy convergence criterion ($\approx 10^{-5}$ meV/supercell) is needed in the electronic loop to get the required accuracy in the Hellmann-Feynman forces. This value is constant for different supercell sizes, since forces are derivatives requiring the same absolute energy convergence. To achieve this high convergence criterion the block-Davidson iteration scheme[38] for electronic minimization is most useful.

As for the supercell size, we consider for each phase 3 different cell sizes with up to 256 atoms (Tab. I). For the phonon dispersion, we find that with two exceptions both phases show a very fast convergence indicating predominant short range interactions. The first, minor exception concerns the fcc $T_1[110]$ branch (cf. Fig. 4) where a known[39] Kohn anomaly causes small deviations from a linear behavior. Corresponding phonon energy differences are, however, very small (<0.5 meV/atom) and

thus barely visible. More importantly they do not affect the resulting quasiharmonic free energy (Tab. I) and thus do not need to be resolved in full detail for our purpose.

The other, much more pronounced exception occurs along the already discussed bcc $T_1[110]$ branch as a consequence of the instability (Fig. 5a). The corresponding dispersion relation is complex in terms of a Fourier expansion. A significant number of Fourier components needs to be included clearly indicating long ranged interactions in real space. Even after stabilization the branch shows deviations from a sinusoidal behavior requiring rather large supercells to capture the exact wave vector dependence. In order to handle this challenging task, we apply a special treatment in describing the phonon dispersion along this branch as discussed in Sec. III F.

Despite the rather strong influence of the supercell size on the phonons in the bcc $T_1[110]$ branch, the resulting quasiharmonic free energy shows again a very small dependence. This issue is illustrated in Tab. I and Fig. 1a. The reason is exactly the same as for the negligible T^{el} dependence discussed above. The weighting factor of the affected region is too small to yield visible effects in the free energy. Based on these findings, we conclude that the exact wave vector dependence of the bcc $T_1[110]$ branch does not need to be resolved for an accurate free energy description. We can thus safely use Fourier interpolations based on the $3\times3\times3$ cell for fcc and the $4\times4\times4$ cell for bcc for our F^{qh} calculations presented in Sec. IV. (The fcc phonon dispersion in Fig. 4 corresponds, however, to a $4\times4\times4$ cell to fully resolve the Kohn anomaly.)

Let us also briefly mention our procedure for the parametrization of the $F^{qh}(V,T)$ surface. The temperature dependence is straightforward since it is contained analytically in Eq. (13). As regards the volume dependence, it has been pointed out in Ref. [14] that various approximations (e.g., linear Grüneisen method) are not sufficient for a high accuracy description. We therefore investigated this issue in detail using up to 10 explicitly calculated volume points in the relevant range. We find that a second order polynomial fit $F^{qh}(V,T) = \sum_{i=0}^{2} c_i(T)V^i$ results in a sufficiently accurate description with an error of below 0.2 meV/atom. This parametrization is thus

applied for the calculations in Sec. IV.

D. Anharmonic vibrations

1. Effect of electronic temperature

The basic equation for the (classical) explicitly anharmonic free energy F^{ah} within the thermodynamic integration scheme reads for a unary crystal[16]

$$F^{\mathrm{ah}}(V,T) = \int_0^1 d\lambda \left\langle F^{\mathrm{el}}_{\mathbf{R}}(V,T^{\mathrm{el}}) - F^{\mathrm{el}}_0(V,T^{\mathrm{el}}) \right. $$
$$\left. - \sum_{k,l} \frac{M}{2} u_k u_l D_{kl}(V,T^{\mathrm{el}}) \right\rangle_{NVT,\lambda} , \quad (16)$$

where $F^{\mathrm{el}}_{\mathbf{R}} = F^{\mathrm{el}}(\{\mathbf{R}_I\})$, $F^{\mathrm{el}}_0 = F^{\mathrm{el}}(\{\mathbf{R}^0_I\})$, $u_k = R_k - R^0_k$, M=atomic mass, and where T^{el} explicitly indicates the dependence on the electronic Fermi broadening. Further, $\langle...\rangle_{NVT,\lambda}$ is the thermodynamic average of a NVT ensemble at a fixed coupling coefficient to the quasiharmonic reference, λ.

The thermodynamic average can be calculated using molecular dynamics (MD) simulations. In such a case there are four distinct ways in which temperature enters Eq. (16): First, it directly controls the thermostat during the MD run (MD temperature: T_{MD}). Second, the electronic temperature/broadening affects the Hellmann-Feynman forces which are used to generate the phase space trajectory (dynamic influence: $T^{\mathrm{el}}_{\mathrm{dyn}}$). We can also describe this as the effect of the electrons on the nuclei thermodynamics (el→nucl anharmonic coupling). Third, the electronic free energy change, $(F^{\mathrm{el}}_{\mathbf{R}} - F^{\mathrm{el}}_0)$, at a certain fixed point $\{\mathbf{R}_I\}$ in ionic configuration space depends directly on T^{el} (static influence: $T^{\mathrm{el}}_{\mathrm{stat}}$). This can be viewed as the reversed effect where the ions affect the electron thermodynamics (nucl→el anharmonic coupling). Fourth, T^{el} influences the reference potential via the dynamical matrix D (reference temperature: $T^{\mathrm{el}}_{\mathrm{ref}}$).

In principle, to guarantee thermodynamic equilibrium at a given temperature T we must ensure that

$$T = T_{\mathrm{MD}} = T^{\mathrm{el}}_{\mathrm{dyn}} = T^{\mathrm{el}}_{\mathrm{stat}}, \quad (17)$$

whereas an arbitrary temperature can be chosen for $T^{\mathrm{el}}_{\mathrm{ref}}$. The latter is a consequence of the unrestricted choice of the reference potential within a thermodynamic integration scheme. However, our results for both calcium phases indicate that in practice Eq. (17) does not need to be satisfied and that

$$T = T_{\mathrm{MD}} \neq T^{\mathrm{el}}_{\mathrm{dyn}} \neq T^{\mathrm{el}}_{\mathrm{stat}} \quad (18)$$

yields accurate anharmonic free energies even if $T^{\mathrm{el}}_{\mathrm{dyn}}$ and $T^{\mathrm{el}}_{\mathrm{stat}}$ vary independently by more than 1000 K. Further, we find that the theoretical invariance with respect to the reference matrix is broken in practice for the bcc

phase. In fact, we need to set $T^{\mathrm{el}}_{\mathrm{ref}} = T^{\mathrm{el}}_{\mathrm{dyn}}$ for efficiency and $T^{\mathrm{el}}_{\mathrm{ref}} = T^{\mathrm{el}}_{\mathrm{stat}}$ for accuracy in order to avoid errors of several meV/atom in the *final* free energy.

To elucidate the effect of Eq. (18) we perform calculations at $T = T_{\mathrm{MD}} = 800$ K and at independently varying $T^{\mathrm{el}}_{\mathrm{dyn}}$ and $T^{\mathrm{el}}_{\mathrm{stat}}$. In particular, we use electronic temperatures of 0 K, 800 K, and 1160 K and we properly treat $T^{\mathrm{el}}_{\mathrm{ref}}$ to avoid the corresponding error at this stage. For the dynamic case, i.e., for varying $T^{\mathrm{el}}_{\mathrm{dyn}}$, we find for both phases that within the statistical error of <0.5 meV/atom the ionic trajectories are insensitive to changes in the electronic temperature. For the static case, i.e., varying $T^{\mathrm{el}}_{\mathrm{stat}}$, we can efficiently reach a higher numerical precision by employing the UP-TILD method (following section). We find differences of less than 0.2 meV/atom for fcc and bcc when changing $T^{\mathrm{el}}_{\mathrm{stat}}$ from 0 K to 1160 K. We can therefore conclude that in calcium there is negligible anharmonic coupling in both directions: el→nucl and nucl→el.

We now turn to the $T^{\mathrm{el}}_{\mathrm{ref}}$ dependence. The above mentioned broken invariance and related errors occur only in the bcc phase. They are related to the peculiarities in the $T_1[110]$ phonon branch, but they are not a direct consequence of the instability. We focus on a specific example to enable a convenient discussion.

Consider the curves represented by open circles (blue, orange, and gray) in Fig. 2. They show the anharmonic free energy for a 54 atomic bcc supercell calculated once with $T^{\mathrm{el}}_{\mathrm{ref}} = 0$ K (gray) and once with $T^{\mathrm{el}}_{\mathrm{ref}} = 1160$ K (blue/orange), but keeping $T^{\mathrm{el}}_{\mathrm{dyn}}$ and $T^{\mathrm{el}}_{\mathrm{stat}}$ in both runs at a fixed temperature of 1160 K. We note differences of up to 3 meV/atom in the absolute value and a strikingly different volume dependence particularly for LDA. Explicit tests show that both of these effects are almost completely due to the electronic temperature dependence of the single exact frequency on the $T_1[110]$ branch (and its symmetric counterparts) captured in the 54 atomic bcc cell (red upper tick labeled "3" in the inset of Fig. 5). This frequency has a relatively strong weighting factor if the free energy is obtained from a coarse grid of exact frequencies. In practicable anharmonic calculations we are, indeed, forced to calculate the free energy on a coarse grid of exact frequencies, since only those frequencies can be described which are contained in the specific supercells.

Next, we need to combine the results for the anharmonic free energy with a corresponding F^{qh} calculation in order to obtain the total vibronic free energy. For F^{qh}, we can and we should use a dense Fourier interpolated mesh in order to guarantee a good sampling of the low energy branches. The different sampling for F^{qh} (mesh frequencies) and F^{ah} (exact frequencies) can, however, result in an error in the final vibronic free energy $(F^{\mathrm{qh}} + F^{\mathrm{ah}})$ if we choose for the bcc phase an inconsistent electronic temperature for the reference potential, i.e., $T^{\mathrm{el}}_{\mathrm{ref}} \neq T^{\mathrm{el}}_{\mathrm{stat}}$. In the present case we find an error of ≈ 3 meV/atom caused by different T^{el} dependencies of the free energy from mesh frequencies and the one from exact frequencies (Fig. 1b). The different T^{el} dependence
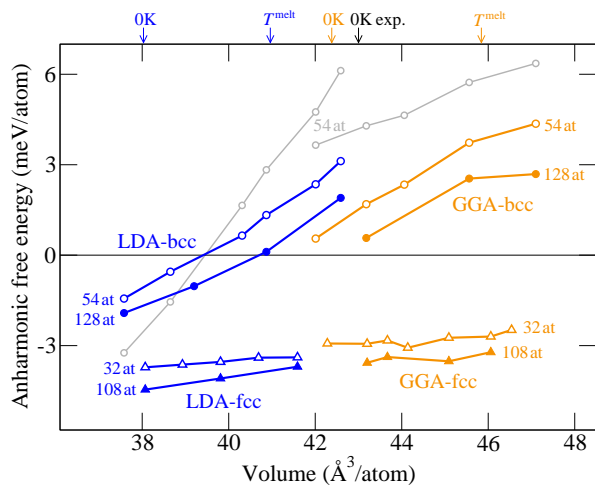
FIG. 2: (Color online) Volume dependence of the anharmonic Helmholtz free energy for both investigated xc functionals (LDA and GGA-PBE) and phases (fcc and bcc). The temperatures are (see main text for details): $T_{\mathrm{MD}} = 800$ K, $T_{\mathrm{dyn}}^{\mathrm{el}} = T_{\mathrm{stat}}^{\mathrm{el}} = 1160$ K, and $T_{\mathrm{ref}}^{\mathrm{el}} = 1160$ K (for blue and orange curves) and $T_{\mathrm{ref}}^{\mathrm{el}} = 0$ K (gray curves). Open circles correspond to a $3\times3\times3$ bcc supercell (54 atoms), closed circles to a $4\times4\times4$ bcc supercell (128 atoms), open triangles to a $2\times2\times2$ fcc supercell (32 atoms), and closed triangles to a $3\times3\times3$ fcc supercell (108 atoms). Statistical errors are of a similar size as the symbols indicating calculated values (not shown). Lines in between symbols are a guide to the eye. The arrows at the top indicate equilibrium volumes at $T = 0$ K and the melting temperature, respectively, for both xc functionals and the experimental $T = 0$ K equilibrium volume.

TABLE II: Optimized UP-TILD parameters for calcium and the corresponding speed ups and UP-shifts $\langle \Delta F^{\mathrm{el}} \rangle^{\mathrm{UP}}$ per atom as compared to a "usual" thermodynamic integration run. Cutoff refers to the employed plane wave cutoff energy and the k-density is given in k-points $\cdot$ atoms.

	fcc calcium				bcc calcium			
	$2\times2\times2$ sc		$3\times3\times3$ sc		$3\times3\times3$ sc		$4\times4\times4$ sc	
	32 atoms		108 atoms		54 atoms		128 atoms	
	low	high	low	high	low	high	low	high
cutoff (eV)	130	170	130	170	130	170	130	170
k-points	2^3	4^3	2^3	3^3	2^3	4^3	Γ	3^3
k-density	256	2048	864	2916	432	3456	128	3456
speed up	$\times\mathbf{15}$		$\times\mathbf{10}$		$\times\mathbf{25}$		$\times\mathbf{40}$	
$\langle \Delta F^{\mathrm{el}} \rangle^{\mathrm{UP}}$	1 meV		1 meV		1 meV		4 meV	

age $\langle ... \rangle_{NVT,\lambda}^{\mathrm{low}}$ by employing Langevin dynamics. In a second step, the high converged thermodynamic average $\langle ... \rangle_{NVT,\lambda}^{\mathrm{high}}$ is obtained by the following upsampling procedure

$$\langle ... \rangle_{NVT,\lambda}^{\mathrm{high}} = \langle ... \rangle_{NVT,\lambda}^{\mathrm{low}} - \langle \Delta F^{\mathrm{el}} \rangle^{\mathrm{UP}}, \qquad (19)$$

where

$$\langle \Delta F^{\mathrm{el}} \rangle^{\mathrm{UP}} = \frac{1}{N} \sum_{\mathbf{R}}^{N} \left(F_{\mathbf{R}}^{\mathrm{el,low}} - F_0^{\mathrm{el,low}} \right) - \left(F_{\mathbf{R}}^{\mathrm{el,high}} - F_0^{\mathrm{el,high}} \right). \qquad (20)$$

The sum runs over N uncorrelated structures (typically $N < 100$) which are extracted from the low converged run; separately for each volume, temperature, and coupling coefficient. For each such structure, $F_{\mathbf{R}}^{\mathrm{el,low}}$ ($F_{\mathbf{R}}^{\mathrm{el,high}}$) denotes the corresponding electronic free energy calculated with low (high) convergence parameters. Further, $F_0^{\mathrm{el,low}}$ and $F_0^{\mathrm{el,high}}$ refer to the electronic free energies of the respective equilibrium structures.

Our optimized values for the UP-TILD method in calcium are given in Tab. II. For both smaller supercells ($2\times2\times2$ for fcc and $3\times3\times3$ for bcc), very efficient low convergence parameters – 20 sec and 80 sec respectively for a single MD step on a AMD Opteron 2.4 GHz with 24 cores – give already an extremely accurate value for F^{ah}. The remaining UP-shift is only $\langle \Delta F^{\mathrm{el}} \rangle^{\mathrm{UP}} = 1$ meV/atom and the corresponding convergence of the sum in Eq. (20) is very quick with $N = 10 \ldots 20$. For the $3\times3\times3$ fcc supercell, we evaluate the possibility to use only the Γ point for the electronic sampling. This, however, turns out to be insufficient for generating a reasonable configuration space distribution and a $2\times2\times2$ k-mesh has to be used instead. In contrast, for the larger bcc supercell, a Γ point calculation is a good starting point for the UP-TILD method, as we verify explicitly, resulting in a remarkable speed up of $\times40$.

As regards the Langevin dynamics, we investigated the important influence of the friction parameter γ over 4 orders of magnitude. We find that $\gamma \leq 0.001$ is significantly

can be understood by considering the effective contribution of the T_1 branch. As mentioned above the weighting factor for this region is relatively strong for the coarse exact frequency grid. In contrast, it is significantly smaller for a dense mesh due to the occurrence of low energy branches in other regions of the Brillouin zone showing a different T^{el} dependence.

We stress that the above effect is not a direct consequence of the instability. In the discussed example we are using the procedure described in Sec. III C 1 to project out the instability region. Therefore the exact as well as mesh frequencies used to calculate the free energy do not contain any imaginary modes. The reason for the strong influence of $T_{\mathrm{ref}}^{\mathrm{el}}$ is rather the peculiar dependence of the *stable* region of the $T_1[110]$ branch on electronic temperature (Fig. 5a).

2. UP-TILD method

A direct high-accuracy calculation of F^{ah} using Eq. (16) is computationally demanding. We employ instead the UP-TILD[14] method which generates in a first step a low converged (e.g., cutoff or k-points, *not* statistics) and therefore efficient thermodynamic aver-

too low to achieve any reasonable statistical convergence. A value of ≥ 0.1 is instead too high resulting in imprecise anharmonic free energies. The best choice turns out to be close to 0.01, a value which has been successfully employed also in a recent aluminum study.[14] The precise value for an optimal γ depends additionally on the MD time step Δt, since it is mainly the product $\gamma \Delta t$ entering the Langevin equations and determining the dynamics. We find that $\gamma \Delta t = 0.01 \cdot 20$ fs and $0.02 \cdot 10$ fs result in similar accuracy and efficiency. Time steps larger than 20 fs should not be used since they fail to sample the high frequency vibrations in calcium and thus lead to wrong free energies.

We sample the MD trajectory at each λ value for up to 50 ps (after equilibration) resulting in general in a statistical error of below 0.5 meV/atom. We are able to efficiently reduce the expensive equilibration time on the actual DFT potential (≈ 1 ps) by employing an inexpensive pre-equilibration on the reference potential (200 ps). Exact equilibration and simulation times depend, however, strongly on temperature and volume since increasing both leads to an increase in the phase space which needs to be sampled. They can also depend on the coupling constant λ with values close to 0 and 1 being particularly difficult to converge statistically. Our largest statistical errors are in the range of 1 meV/atom for a single λ value. Note, however, that this error does not translate into an equivalent error in the final anharmonic free energy since the latter is averaged out and thus reduced by performing the λ integration.

Concerning the λ integration, we performed detailed investigations using a mesh of up to 11 explicitly calculated λ points $(0, 0.1, \ldots, 1)$. For the fcc phase, we find that the thermodynamic average $\langle \ldots \rangle_{NVT,\lambda}$ obeys a nearly linear dependence (cf. circles in Fig. 3a) as similarly found for instance in fcc aluminum.[14] In fact, our results indicate that we might replace the full λ integration by considering a single value at $\lambda = 0.5$, while loosing only $1 \ldots 2$ meV/atom in precision. To keep our desired accuracy goal we, however, refrain from a linear approximation and capture instead the full dependence on a dense λ mesh of 6 equidistantly distributed points.

The situation turns out to be more involved for the bcc phase. We find the linear approximation to cause deviations of up to 20 meV/atom. In particular, the λ region close to zero shows a strongly increasing dependence as illustrated by the example in Fig. 3a (squares). The strength of the increase at $\lambda = 0$ depends not only on volume and temperature but also on the quasiharmonic reference matrix. Using an inconsistent electronic temperature for the reference matrix (e.g., $T_{ref}^{el} = 0$ K but $T_{dyn}^{el} = T_{stat}^{el} = 1160$ K) results in a significantly stronger increase than for a consistent one. In agreement with the discussion in Sec. III D 1 this indicates that a consistent electronic temperature is physically more sound and technically more efficient. However, even for the consistent case we find a strongly non-linear behavior of the thermodynamic average in bcc making an accurate and
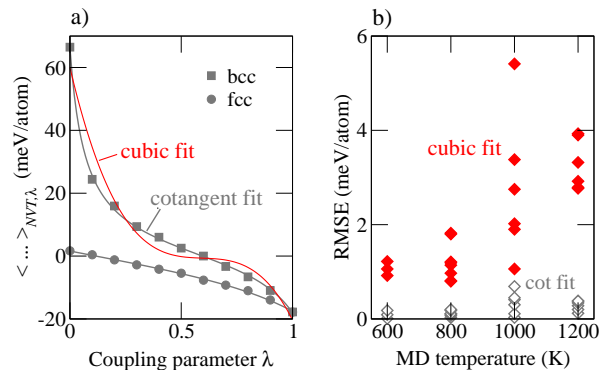

FIG. 3: (Color online) Illustration of the performance of the fit based on Eq. (21). In a) the λ-dependence of the thermodynamic average $\langle \ldots \rangle_{NVT,\lambda}$ is shown for a fcc and bcc structure both at an MD temperature of 1000 K. Gray lines indicate a fit based on Eq. (21) and the red line is a 3rd order (cubic) polynomial fit. In b) the root-mean-square error (RMSE) of the explicitly calculated points from the respective fit is shown for the bcc structure at various MD temperatures. At a single temperature different points correspond to different lattice constants.

efficient λ integration challenging.

A natural possibility to deal with this issue seems to be an extension of the linear fit by including higher order polynomials. However, we find this ansatz to show only slow convergence with the number of polynomials included. Based on our large set of calculated data, we are able to derive a much more efficient way. Our ansatz assumes the following fit

$$\langle \ldots \rangle_{NVT,\lambda} = a_0 \cot[\pi(a_1\lambda + a_2)] + a_3 \qquad (21)$$

involving four fitting parameters $a_0 \ldots a_3$. Its performance should be therefore compared to a polynomial with the same number of parameters, i.e., a cubic polynomial. A specific example clearly showing how well the λ dependence of the thermodynamic average is described by Eq. (21) is given in Fig. 3a. In contrast, the cubic fit introduces oscillations which are too strong causing maximum deviations from the true points of up to 10 meV/atom. The behavior found in this example turns out to be a general feature in the Ca bcc phase as demonstrated by the root-mean-square deviations displayed in Fig. 3b. Moreover, we can safely extend the cotangent fit to describe also the smooth λ dependence of the Ca fcc phase, since it is similarly well described (Fig. 3a). In summary, we use the cotangent fit Eq. (21) and a converged λ mesh of six equidistant points $(0, 0.2, 0.4, 0.6, 0.8, 1)$ for each considered volume and temperature on both the fcc and bcc anharmonic free energy surface.

We next describe our procedure for parametrizing F^{ah} as a function of volume and temperature. A detailed discussion of the corresponding difficulties has been given in Ref. [14]. A solution has been proposed which uti-

lizes a modified version of Eq. (13) as the fitting func-
tion and a renormalized average frequency as the fitting
parameter.[14] We find this approach also well suited for
describing F^{ah} in the present case (both fcc and bcc). We
need, however, to extend it slightly in order to accurately
take the supercell size convergence into account, which is
computationally prohibitive by direct calculation.

Our procedure is as follows: In a first step, we calcu-
late a dense (V, T)-mesh of ≈ 20 F^{ah} points in the rele-
vant range for the two smaller supercells ($2\times2\times2$ for fcc
and $3\times3\times3$ for bcc). We then employ the fit proposed in
Ref. [14] using in particular a renormalized anharmonic
frequency expanded as $\omega^{\mathrm{ah}} = a_0 + a_1 T + a_2 V$, where a_0,
a_1, and a_2 are fitting coefficients. The root-mean-square
error of this fit from the explicitly calculated values is
well below the statistical uncertainty. Next, we calculate
a much coarser grid of 3 to 4 volumes at a fixed temper-
ature (close to the transition temperature; see Fig. 2) for
the larger supercells ($3\times3\times3$ for fcc and $4\times4\times4$ for bcc).
We find the difference between the free energies of the
larger and the smaller supercells to be ≈ 1 meV/atom for
fcc and ≈ 2 meV/atom for bcc and nearly volume inde-
pendent. We parametrize this difference using $\omega^{\mathrm{ah}} = a_0$.
Despite the fact that ω^{ah} is volume and temperature in-
dependent, the resulting anharmonic free energy contains
both dependencies through the specific form of the fitting
function.[14] In a last step, the fitted difference is added
on top of the parametrization for the smaller supercells
and the resulting sum constitutes our final anharmonic
free energy surface.

We conclude with a comment on the expected over-
all precision in F^{ah}. From a statistical viewpoint, we
can confidently claim to be converged to well below
1 meV/atom. The reason is the fact that each surface is
assembled from a large multitude of *statistically indepen-
dent* runs with each run being well converged by itself.
Moreover, we have accurate parametrizations available
which tend to average out the individual statistical er-
rors. Further, we know that we are well converged in
terms of plane wave cutoff and k-points by employing
the UP-TILD method. The most difficult estimation is
related to the remaining error due to the supercell size.
For the investigated supercell sizes we see differences of
up to 2 meV/atom. In general, we expect anharmonic in-
teractions to be short ranged in real space. In the present
case, this is additionally supported by the dominating
short ranged character of the quasiharmonic interactions
(see discussion in Sec. III C). We thus estimate that a fur-
ther increase in supercell size will result in changes signif-
icantly lower than found for the investigated supercells.
Additionally, we find a similar supercell size convergence
for both phases (Fig. 2) and expect this to reduce further
the error in the free energy difference between bcc and
fcc which is our main target. In total, we conjecture our
error in F^{ah} to be below 1 meV/atom.

E. Vacancies

The Gibbs energy of vacancy formation is obtained as

$$G^{\mathrm{f}}(P, T) = F^{\mathrm{v}}(\Omega_P, T; N^{\mathrm{v}}) - N^{\mathrm{v}} F^{\mathrm{p}}(V_P, T) + P v^{\mathrm{f}}, \quad (22)$$

where F^{v} is the free energy of a vacancy supercell with
N^{v} atoms and at supercell volume Ω_P which is adjusted
such as to guarantee the same P as in the perfect bulk.
Further, F^{p} is the free energy per atom of the perfect
bulk calculated at atomic volume V_P corresponding to
pressure P and $v^{\mathrm{f}} = \Omega_P - N^{\mathrm{v}} V_P$ the volume of va-
cancy formation. Similar to what is found for instance
in Ref. [40], our calculations also show the importance
of the $P v^{\mathrm{f}}$ term in Eq. (22) which – even for moderate
pressures – can modify G^{f} by a few tenths of meV. In
particular, for ambient pressure conditions of 0.1 GPa
we find an increase of G^{f} by ≈ 20 meV/atom. However,
the effect on the total Gibbs energy $G(P, T)$ in Eq. (6)
is strongly suppressed due to the exponential function in
Eq. (7) and at most notable in derivatives such as the
heat capacity.

We calculate for F^{v} the full set of excitations as pro-
vided in Eq. (5). We focus specifically on the $2\times2\times2$
supercell for fcc and the $3\times3\times3$ supercell for bcc. In
the first place, all internal degrees of freedom are fully
relaxed for each cell and at each volume. Starting from
the relaxed geometries, the calculation of the various free
energy contributions for the vacancy supercell proceeds
as described in the previous sections for the perfect bulk.
In particular we use the same convergence parameters.
Special care must be, however, taken in the case of the
quasiharmonic contribution, in order to guarantee a con-
sistent treatment between the vacancy and perfect bulk.
We accomplish this by employing the correction scheme
given in Ref. [14].

In our MD simulations for the anharmonic contribu-
tion to the vacancy supercell, we experience an increased
mobility of the vacancy, i.e., a hopping from its original
site to neighboring sites, when looking at high temper-
atures and λ values close to 1. Further, we find that
the mobility is stronger in the bcc than in the fcc phase
which is intuitive due to the more open structure. In
order to guarantee a correct calculation of F^{ah}, all con-
figurations at which the vacancy has left its original place
need to be carefully extracted and removed from the ther-
modynamic average. The reason is that our reference dy-
namical matrix has a fixed and unmovable position for
the vacancy. In order to determine vacancy motion, we
carefully monitor the next nearest neighbors of the va-
cancy during an MD run. If we encounter an atom being
closer to the vacancy equilibrium position than to its own
equilibrium position, we define this configuration as a va-
cancy movement and take the corresponding part of the
MD trajectory out of the average procedure. Our results
indicate that the employed extraction procedure is well
defined, since we find the atoms to be in general vibrating
close to their equilibrium positions – even for high tem-
peratures and λ close to 1 – and the vacancy movement

to be a singular and clearly identifiable process.

We conclude with comments on the expected overall precision in the total Gibbs energy due to vacancies, i.e., the $-c^{eq}k_B T$ term in Eq. (6). Focussing first on the temperature region relevant for the phase transition (716 K) we find vacancy concentrations which are well below 10^{-4} for all phases. The corresponding contribution to the total Gibbs energy is, as a consequence, fully negligible (< 0.01 meV/atom). In such a case also convergence issues do not play any role and we can safely conclude that the final Gibbs energy difference between bcc and fcc is highly accurate with respect to vacancies.

The only relevant contribution due to thermally excited vacancies reveals itself in the high temperature heat capacity (Fig. 10b) in the bcc phase. While the absolute Gibbs energy is still very small (< 0.2 meV/atom) the exponential decrease results in a small yet visible heat capacity contribution. We have not explicitly considered a larger supercell than the 54 atomic $3{\times}3{\times}3$ bcc supercell for the vacancy calculations. Based on our previous experience where we found negligible differences when increasing from 32 to 108 atoms in fcc aluminum,[14] we expect, however, also negligible influences in the present case.

In fact, the crucial point to note is that the qualitative result obtained in Sec. IV E which distinguishes between the two sets of experimental data cannot be altered by larger vacancy supercell sizes. To see this note that the contribution of vacancies to the total Gibbs energy has always an exponential temperature dependence. This dependence reveals itself in a strongly non-linear behavior of the heat capacity. The upper experimental set of data (Fig. 10a) shows however a perfectly linear behavior and thus vacancies are clearly ruled out as a possibility to shift the heat capacity curve from the lower experimental set of data to the upper one.

F. $T_1[110]$ bcc instability

The focus of this section is to describe the special treatment utilized in determining the $T_1[110]$ branch in the bcc phonon dispersion (Fig. 5a). Additionally, we want to lay out our procedure for capturing qualitatively the influence of phonon-phonon interactions on the instability in the GGA $T_1[110]$ branch and describe the calculations for the long wave length limit (shear of the bcc cell).

To see in detail the difficulties related to the $T_1[110]$ branch consider the inset in Fig. 5a focussing on the GGA phonon dispersion at $T^{el}=0$ K (solid orange line). Note next the upper red ticks indicating the exact phonon wave vectors which are contained in supercells practically accessible in a quasiharmonic calculation. The important point to note is that none of these exact wave vector grids is fine enough to resolve the instability, i.e., even for the $5{\times}5{\times}5$ supercell both of the exact wave vectors lie outside the instability region. As a consequence, also the resulting Fourier interpolation based on these exact

frequencies cannot resolve the instability correctly.

An extension of the supercell to sizes which provide a sufficient number of exact wave vectors in the instability region is clearly not feasible in full 3D. One possible solution would be an application of the linear response method in reciprocal space, which does not require large supercells.[41] In the present case, however, a much more direct approach is feasible in real space. The important point to realize is that the [110] direction corresponds in real space to an elongation of the primitive bcc cell only along a single direction. For instance, in order to achieve the dense mesh of 15 exact wave vectors shown at the bottom of the inset of Fig. 5a, we need a supercell of $29{\times}1{\times}1$ in terms of the primitive bcc cell containing merely 29 atoms. Note that the remaining exact points are lying in the other half of the [110] direction, i.e., the direction from N back to Γ. Besides the extended supercell the calculation proceeds otherwise as within a "usual" quasiharmonic setting. We stress in particular that, within the quasiharmonic regime, the described approach does not entail any additional approximation, since the phonons are non-interacting and each branch can be therefore described separately.

We investigated various supercells up to the above mentioned one with 29 atoms. We find that the instability region at various electronic temperatures is well described (deviation < 0.3 meV) by a supercell containing 19 atoms. We use therefore this supercell for the next task of estimating the qualitative influence of phonon-phonon interactions on the instability. In particular, we use for that purpose the following approach.

In a first step, we use an MD simulation in the elongated supercell to generate a configuration space distribution. The exact temperature controlling the MD simulation is of minor relevance since we only aim at a qualitative description. Out of the generated distribution, we extract a set of uncorrelated snapshots and calculate for each the corresponding dynamical matrix. Next, we average over the various obtained dynamical matrices which (if convergence is achieved) restores the original bcc symmetry. In a final step, we calculate the phonon dispersion for the average dynamical matrix.

The described approach takes into account phonon-phonon interactions only among phonons along the [110] direction, while obviously completely neglecting the interactions with any other phonon in the full 3D Brillouin zone. Therefore, the obtained results cannot be used quantitatively, in particular, for calculating an anharmonic free energy. We expect, however, that the qualitative result that phonon-phonon interactions result in a stabilization of the instability (see gray line in the inset of Fig. 5a) does indeed hold.

In order to study the long wave length limit of the instability, we shear the primitive bcc unit cell modifying a single vector. In particular, if $\mathbf{a}_1$, $\mathbf{a}_2$, and $\mathbf{a}_3$ denote primitive bcc vectors, the vectors of the sheared cell are obtained by $\mathbf{a}'_1 = \mathbf{a}_1 + \delta\mathbf{a}_2 - \delta\mathbf{a}_3$, $\mathbf{a}'_2 = \mathbf{a}_2$, and $\mathbf{a}'_3 = \mathbf{a}_3$, with δ measuring the strength of the shear (Fig. 5b). This

shear corresponds exactly to the long wave length limit of the $\langle 1\bar{1}0 \rangle$ polarization of the transversal branch along the Γ to N direction, which is commonly labeled $T_1[110]$. To study the influence of the electronic temperature on the energy of the sheared unit cell, we use a plane wave cutoff of 150 eV and 16,420 k-points in the irreducible Brillouin zone (convergency better than 0.1 meV/atom). For the pressure related investigations, we use a PAW potential including additionally the $3s^2$ orbitals (10 valence electrons) to avoid an error of a few meV/atom. The plane wave cutoff for this potential is set to 310 eV. The electronic density of states calculations (Fig. 5c) are based on the same settings which guarantees converged results particularly due to the high k-point sampling. We also use a convolution with a Gaussian function with a width of 0.1 eV to smoothen the density of states.

IV. RESULTS

Any free energy study relies on accurate $T=0$ K calculations. Table III summarizes our respective results for fcc and bcc calcium and we first discuss the performance of the employed PAW potentials.

The enthalpy difference $\Delta H^{\text{bcc}-\text{fcc}}$ is extremely well described showing deviations of only 0.1 meV/atom with respect to the most accurate all-electron methods available, FLAPW and FPLMTO. For the equilibrium lattice constant we find a small underestimation of 0.09% (0.05%) for LDA (GGA) by the PAW potential. This is directly related to a small overestimation of the bulk modulus and its derivative. To check the influence of these deviations at finite temperatures, we combine the all-electron $T=0$ K curve with finite temperature excitations from PAW. We find changes of 0.3 meV/atom in the Gibbs energy at the phase transition temperature. These changes are the same for fcc and bcc so that the corresponding difference is not affected. We therefore conclude that the employed PAW potentials are well suited for the present high accuracy study.

Focussing now on the comparison with experiment for the fcc phase, we discover two interesting facts: 1) For LDA, we find the well known[9] underestimation of the experimental lattice constant due to overbinding. GGA generally overestimates the equilibrium lattice constant.[9] For fcc calcium, we have the rare situation that also GGA underestimates the lattice constant (albeit by 0.5% only). 2) Except for the lattice constant/volume, we face the untypical circumstance that the scatter in experimental data is of the same order as the deviation between LDA and GGA. A comparison at this point stays therefore inconclusive.

A. Stabilization of the $T_1[110]$ bcc instability

Before discussing the instability occurring in bcc, let us first turn to the phonon dispersion of the low temperature
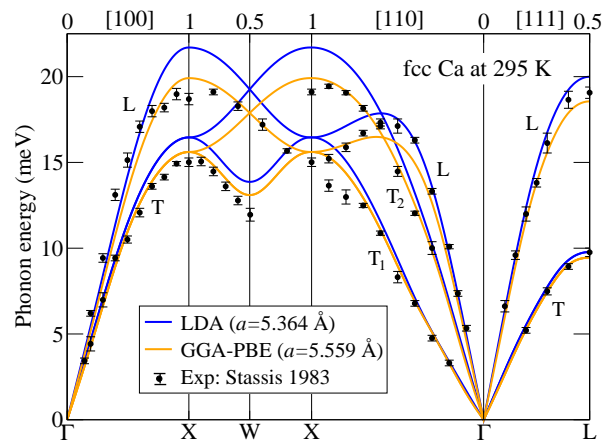

FIG. 4: (Color online) Phonon dispersion of fcc Ca at 295 K along high symmetry directions. The corresponding lattice constant a for the theoretical calculations (LDA and GGA-PBE) is shown in the legend. The T_1 and T_2 branches correspond to the $\langle 1\bar{1}0 \rangle$ and $\langle 001 \rangle$ polarization, respectively. The experimental data including error bars are from Ref. [39].

fcc phase for which experimental data are available and an evaluation of the performance of the xc functionals can be done.

The fcc phase shows a phonon dispersion (Fig. 4) typical for elements with predominantly nearest neighbor interactions.[9] Our theoretical results are in good agreement with experimental values. In particular, the GGA functional shows a very good performance over almost the entire Brillouin zone. The LDA functional results in a qualitatively similar phonon dispersion as the GGA functional (i.e., showing the same phonon wave vector dependence). It produces, however, phonons that are quantitatively roughly 1.07 times higher in energy than GGA. This observation is consistent with trends found in a wider range of materials provided that the phonon dispersion is calculated at the self consistent theoretical lattice constant.[9] It is related to the above mentioned underestimation of the experimental lattice constant by the LDA functional which is particularly large for fcc Ca (Tab. III).

Having established the theoretical accuracy, we turn now to the phonon dispersion of the high temperature bcc phase. It is physically more interesting and challenging than the fcc phase due to the instability region in the $T_1[110]$ branch and its strong coupling to electronic excitations. Our results shown in Fig. 5a reveal in general the same quantitative trend that LDA produces significantly harder phonons. Qualitatively, LDA and GGA show exactly the same phonon wave vector dependence except for the $T_1[110]$ branch. There GGA shows the already mentioned dynamical instability, whereas LDA has a fully stable $T_1[110]$ branch.

The phonon dispersions marked by solid lines in Fig. 5a are obtained at an electronic temperature of zero Kelvin. The dashed and dotted lines show instead the impor-

TABLE III: Equilibrium $T=0$ K properties of fcc and bcc calcium: ΔH=bcc-fcc enthalpy difference, a=lattice constant, V=volume, B=bulk modulus, B'=derivative of B with respect to pressure, and H^{f}=formation enthalpy of the vacancy. All values include zero-point vibrations. For FLAPW and FPLMTO, the latter are taken from the PAW results. Experimental values for ΔH correspond to $T=0$ K and are obtained from the CALPHAD parametrization of Saunders et al.[42] and the parametrization from the SGTE unary database[43] (see also Fig. 6 and corresponding caption). The experimental lattice constant/volume is the $T=0$ K value reported in Ref. [44]. The experimental bulk moduli and derivatives are room temperature values from Refs. [44–48]. A correction of the bulk moduli to $T=0$ K is performed based on the temperature dependence from Ref. [44], but turns out to be irrelevant as compared to the scatter between the different measurements.

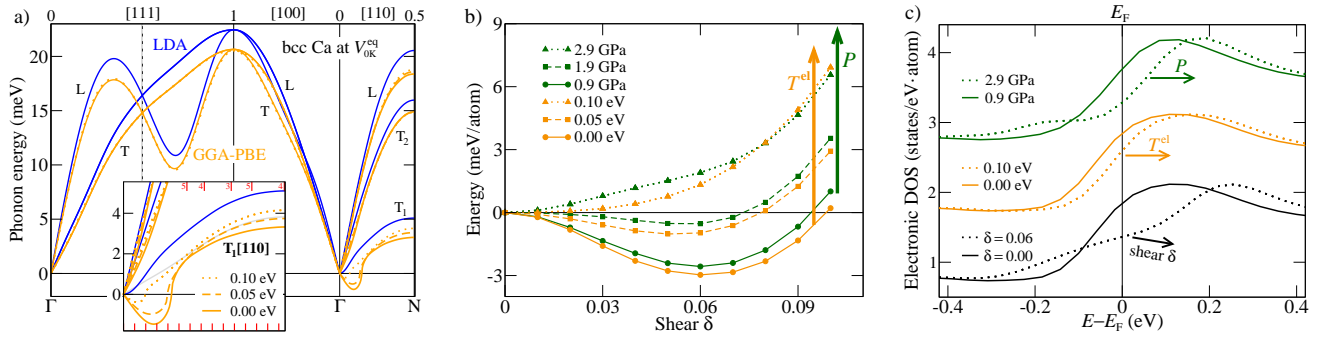| | fcc calcium | | | | | | bcc calcium | | | |
| | LDA | | Exp. | GGA-PBE | | | LDA | | GGA-PBE | |
	PAW	FLAPW		PAW	FLAPW	FPLMTO	PAW	FLAPW	PAW	FLAPW
ΔH (meV)	9.2	9.2	**9.6 … 15**	16.5	16.6	16.5				
a (Å)	5.339	5.344	**5.564**	5.533	5.535	5.535	4.215	4.219	4.390	4.392
V (Å^3)	38.04	38.15	**43.07**	42.35	42.41	42.40	37.44	37.56	42.30	42.35
B (GPa)	18.5	18.1	**15 … 20**	17.2	17.2	17.1	19.1	19.0	15.8	15.6
B'	2.7	2.4	**2.5 … 3.9**	3.3	3.2	3.2	4.0	3.7	2.3	2.1
H^{f} (eV)	1.19			1.16			0.91		0.84	

FIG. 5: (Color online) Analysis of the dynamical instability in the calcium bcc phase. a) Phonon dispersion for LDA and GGA-PBE at the consistent $T=0$ K equilibrium volume V_{0K}^{eq} (Tab. III). Solid lines show results for $T^{\mathrm{el}}=0$ K and dashed and dotted lines for two increased electronic temperatures (GGA-PBE only). The inset enlarges the [110] direction with the upper red ticks indicating exact wave vectors for the bcc supercells used in the quasi/anharmonic calculations (numbers correspond to the three bcc supercells given in Tab. I) and with the lower red ticks indicating the exact wave vectors employed in the special treatment of the T_1[110] description (Sec. III F). The gray line shows the qualitative result of phonon-phonon interactions on the instability (Sec. III F) for GGA-PBE at an MD temperature of 250 K. The T_1[110] branch corresponds to the $\langle 1\bar{1}0\rangle$ polarization, whereas T_2[110] to the $\langle 001\rangle$ one. b) Effect of electronic temperature T^{el} and applied hydrostatic pressure P (the other parameter being kept fixed at zero respectively) on the GGA-PBE energy dependence for a shear of the unit cell δ corresponding to the long wave length limit of the T_1[110] branch in a) (see Sec. III F for definition of δ). The applied pressures of 0.9 GPa, 1.9 GPa, and 2.9 GPa correspond to lattice constants of 4.3 Å, 4.23 Å, and 4.175 Å, respectively. c) Effect of electronic temperature T^{el}, applied hydrostatic pressure P, and of the shear δ on the electronic density of states close to the Fermi level E_{F}. The curves for T^{el} and P are shifted up for clarity by 1 and 2 states/eV·atom, respectively.

tant influence of electronic excitations by displaying the phonon dispersion at Fermi broadenings of 0.05 eV ($\widehat{=}580$ K) and 0.1 eV ($\widehat{=}1160$ K). We observe that upon increasing the electronic temperature the instable phonon branch is lifted up becoming nearly stable at 0.1 eV. Note two important points: 1) The T_1[110] branch is the only branch being visibly affected by electronic temperature. The other branches have almost no dependence. 2) The whole branch containing the instability is affected even in regions where it is actually stable (see, e.g., N point).

To gain further insight, we resolve the instability and

its temperature dependence by following the corresponding modes on the energy surface. We perform such calculations for various instable wave vectors and show a representative example in Fig. 5b corresponding to the long wave length limit. We observe that the energy dependence describes a double well potential which is characteristic for instabilities. The depth of the minimum is rather small in the range of 3 meV/atom below the fully symmetric bcc structure. The displayed energy dependence shows the deepest minimum among all instable wave vectors.

The stabilizing effect of electronic temperature can be

clearly seen also for the energy dependence in Fig. 5b. We perform further investigations to elucidate the physical background for this behavior. We find that a very similar effect of stabilization can be obtained by applying external hydrostatic pressure on the system, i.e., compressing to smaller volumes. In particular, we find that a step size of 1 GPa corresponds to a similar energy shift as one obtained by increasing T^{el} by 0.05 eV (see Fig. 5b). Incidentally, the correspondence with pressure explains why LDA shows no instability at $T^{\mathrm{el}}=0\,\mathrm{K}$ in contrast to GGA. The above mentioned strong underestimation of the equilibrium volume by LDA produces an internal pressure in the system (quantified in the higher bulk modulus). This internal pressure has the same effect as the external pressure applied to the GGA system. (Note that the total pressure is necessarily zero if the system is at equilibrium. It is, however, not the total pressure which is relevant here, but only the pressure contribution caused by the ionic vibrations, i.e., thermal pressure, and the latter turns out to be indeed much stronger for LDA than for GGA as shown explicitly in Fig. 9.)

We are able to further trace back the origin of both influences and relate them to the electronic density of states close to the Fermi level (Fig. 5c). We observe that both, the electronic temperature and pressure, lead to the same changes in the electronic density of states. In particular, we note that the qualitative shape of the latter stays almost unaffected, the dominating effect being instead a shift of the Fermi level to lower energies. This leads to a reduction of electrons at the Fermi level and thus to a stabilization effect.

By pushing the analysis further we can also show that a similar effect on the electron density of states is caused by following the energy along an instable mode (lowest/black curves in Fig. 5c). This time, however, the changes are stronger affecting also the qualitative shape of the density of states. At low electronic temperatures and pressures the instability therefore succeeds over the other two effects leading to stabilization of the unsymmetric structure. At higher electronic temperatures and pressures the situation changes, but the energetically lowest structure is determined by a much more subtle interplay and coupling between the various influences.

B. The fcc to bcc transition including all relevant excitation mechanisms

Let us focus now on the fcc to bcc transition. There are two important points distinguishing the present study from previous ones (e.g., Ref. [4]): We include all free energy contributions that might be relevant for the transition, in particular the explicitly anharmonic part of the vibronic motion. We further guarantee the error to be below 0.5 meV/atom for the standard contributions and below 1 meV/atom for the anharmonicity. These two points are crucial because they allow to correlate remaining disagreement with experiment with an error coming
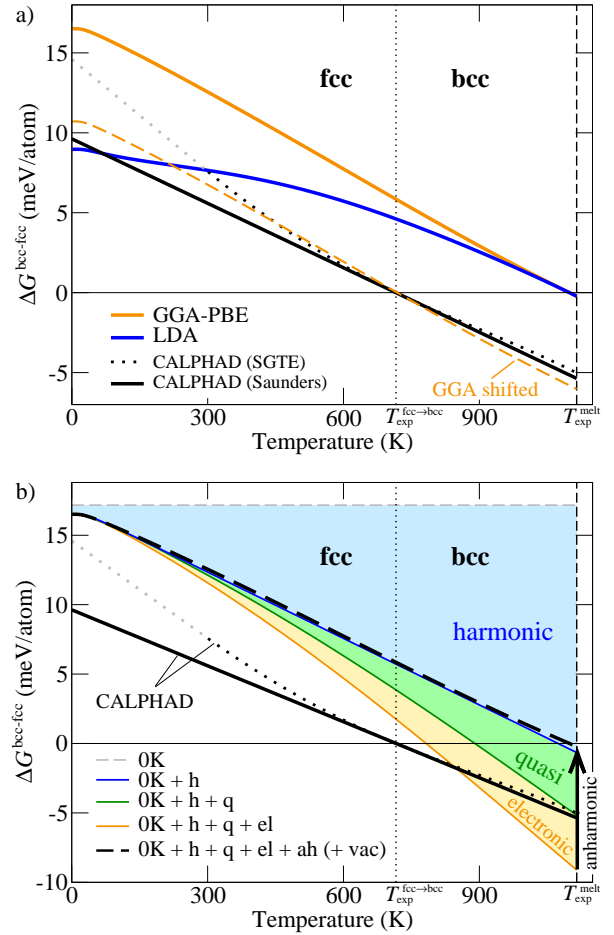

FIG. 6: (Color online) a) Gibbs energy difference between bcc and fcc $\Delta G^{\mathrm{bcc-fcc}}$ at ambient pressure (0.1 GPa). The orange dashed line corresponds to the GGA-PBE result shifted by -6 meV/atom. The vertical lines indicate the experimental fcc to bcc transition temperature[31] $T^{\mathrm{fcc \to bcc}}_{\mathrm{exp}} = 716\,\mathrm{K}$ and melting temperature[31] $T^{\mathrm{melt}}_{\mathrm{exp}} = 1115\,\mathrm{K}$. CALPHAD values are obtained from Saunders et al.[42] and from the SGTE unary database.[43] The gray dotted line indicates a linear extrapolation of the SGTE data[42] to $T=0\,\mathrm{K}$, since the original parametrization diverges at low temperatures. b) Influence of the various Gibbs energy contributions on the GGA-PBE phase transition: 0K=$(T=0\,\mathrm{K})$ enthalpy difference, h=harmonic, q=quasi, i.e., expansion influence, el=electronic, ah=anharmonic, and vac=vacancies.

solely from the xc functionals.

Our results for the Gibbs energy difference between bcc and fcc including all excitations are shown in Fig. 6. Both functionals, LDA and GGA, overestimate the experimental transition on the energy scale by ≈ 6 meV/atom. This rather small energy difference results, however, in an extremely large overestimation of ≈ 400 K on the temperature scale. Note that the energy scale does not relate to the temperature scale in terms of thermal energy, i.e., $E = k_{\mathrm{B}}T$ (6 meV/$k_{\mathrm{B}} \approx 70$ K). The reason is that we are here considering temperature dependent Gibbs en-

ergy differences between phases.

Despite the 6 meV shift with respect to experiment, we find that the GGA approximation shows a Gibbs energy difference which has a very similar slope to that of the CALPHAD data. This is particularly true for temperatures above ≈ 400 K, whereas for lower temperatures, the slopes differ slightly. One should not, however, correlate the disagreement at lower temperatures with a DFT deficiency. At such low temperatures, particularly below room temperature, the CALPHAD Gibbs energies are based on extrapolations of experimental data. This is even true for stable phases, the reason being long equilibration times making calorimetric experiments challenging. Even more, for unstable phases such as bcc, the Gibbs energies are based on extrapolations from their stable regime (either temperature or concentration stabilized). These circumstances make the CALPHAD data at low temperatures questionable especially considering the small Gibbs energy differences being relevant. In fact, this statement is directly supported by noting the inherent inconsistency (several meV/atom) between the two available datasets for calcium (cf. dotted and solid black lines in Fig. 6.).

An interesting observation follows from a comparison of the Gibbs energy difference between the two xc functionals. At $T=0$ K, we have a difference of 6 meV/atom between LDA and GGA, which as discussed above is very relevant in terms of the temperature scale. Nevertheless, at higher temperatures the Gibbs energies of both functionals converge and show a transition at almost exactly the same temperature. The reason for this behavior is that the vibronic contributions compensate the initial $T=0$ K difference. It might be tempting to suppose a systematic physical origin being responsible for the equality in transition temperature between the functionals due to this surprising agreement. So far we have, however, no evidence that this behavior is not pure coincidence.

Fig. 6b shows the individual contributions to the transition arising from the various excitation mechanisms (GGA functional). The largest finite temperature effect is clearly caused by harmonic excitations (light blue shaded). This contribution is obtained by calculating non-interacting phonon energies and the resulting (Helmholtz) free energy at the fixed, for each phase (fcc and bcc) self-consistently obtained $T=0$ K equilibrium volume. As temperature increases, the bcc phase is significantly stabilized by harmonic excitations over fcc as can be intuitively explained by the more open geometry when compared to the close packed fcc structure.

The light green shaded region labeled "quasi" corresponds to the contribution where the fixed volume restriction is lifted and the non-interacting phonons are allowed to vary along the thermal expansion. The thermal expansion is calculated for each phase self consistently and at a fixed pressure, i.e., the result is a Gibbs energy. The pressure corresponds to ambient conditions to allow a consistent comparison with CALPHAD. We find that the quasi contribution also favors bcc over fcc but by a

1/3 smaller amount. The argument for this behavior is the same as above. The light orange shaded region in Fig. 6b indicates the influence of electronic excitations. They also favor bcc over fcc and in fact show a very similar influence as the quasi contribution.

We now focus on the remaining two excitation mechanisms: vacancies and anharmonicity. While vacancies turn out to be irrelevant for the phase transition, the anharmonic excitations, i.e., phonon-phonon interactions, produce a crucial and possibly unexpected effect. Their contribution is indicated in Fig. 6b by the black arrow pointing upwards. It turns out that – against a possible intuitive expectation and opposed to all before discussed contributions – anharmonicity favors the fcc over the bcc phase. What is even more striking is that the magnitude of this contribution is rather large and that it nearly exactly cancels the electronic and quasi contribution over the whole temperature range. Considering Fig. 2, we can resolve the anharmonic excitations for each phase separately. We see that the bcc phase has a positive anharmonic contribution (particularly for GGA). In contrast, the fcc phase has a comparatively strong negative anharmonic contribution over the full volume range. We conclude that the anharmonic stabilization of fcc over bcc is due to phonon-phonon interactions which soften the original non-interacting phonon frequencies in fcc but harden them in bcc.

We finish this section with a crucial observation regarding the effect of the individual excitations on the phase transition and the comparison with experiment. Let us for that purpose single out two quantities capturing the major part of the involved physics: The slope of the Gibbs energy difference in the vicinity of the transition and its actual value at the transition temperature. Both the quasi and the electronic excitations significantly shift the actual Gibbs energy value at the transition temperature towards the experimentally represented curve (CALPHAD). However, for the slope we observe the opposite trend, i.e., it is becoming more negative and thus the disagreement with experiment becomes larger. In contrast, anharmonicity does the following: it carries the actual value at the transition temperature away from experiment, but pushes the slope strongly towards the one seen in the CALPHAD curve.

This behavior is very reasonable: the absolute value of the Gibbs energy difference at the experimental transition temperature is directly related to the energy difference at $T=0$ K and we in fact expect the largest error to originate from the latter. The reason is that this energy difference involves large geometric differences, i.e., a relatively open structure for bcc and a close packed structure for fcc. The slope of the Gibbs energy difference is instead fully related to finite temperature excitations which are eventually based on energy differences stemming from small geometrical distortions. We therefore indeed expect the error related to temperature changes to be much smaller than the one related to the $T=0$ K phase differences.

C. Similarity in the electronic free energy dependence for LDA and GGA

Let us go back to the Gibbs energy difference $\Delta G^{\mathrm{bcc-fcc}}$ containing all excitation mechanisms. Taking a closer look at lower temperatures, we note that the curve for LDA (blue solid line in Fig. 6) has a different dependence than for GGA (orange solid line). In particular, $\Delta G^{\mathrm{bcc-fcc}}$ for LDA shows a small dip at around 100 K, while GGA behaves smoothly. The LDA dependence is not a technical artefact but rather a consequence of an important physical effect. By tracing back the origin we will identify that both xc functionals obey a very similar free energy vs. volume dependence on an absolute scale.

To start off we consider again the LDA $\Delta G^{\mathrm{bcc-fcc}}$ (solid curve in Fig. 7a), but now in comparison with the bcc-fcc Gibbs energy difference *excluding* electronic excitations (dashed curve). The latter difference has an almost perfect linear dependence and we can therefore directly correlate the dip with electronic excitations. In fact, we can even go further and identify the particular phase being mainly responsible for the unusual electronic Gibbs energy dependence. For that purpose, Fig. 7a contains additionally the electronic Gibbs energy for fcc and bcc separately (dotted curves). One can see that the fcc curve decreases faster at low temperatures, but – due to its stronger curvature – bcc overtakes at around the experimental transition temperature. To understand the different dependencies of fcc and bcc, we need to resolve the Helmholtz free energy as a function of volume and temperature, i.e., we need to consider the full electronic free energy surface $\widetilde{F}^{\mathrm{el}}(T, V)$.

We therefore plot a two dimensional projection of a representative set from $\widetilde{F}^{\mathrm{el}}(T, V)$ for fcc and bcc in Fig. 7b and c (blue curves). One can see an important difference: While fcc has almost no volume dependence at any temperature, bcc shows a Helmholtz free energy decreasing with volume and with the decrease becoming stronger as temperature rises. This insight suffices to understand the dependencies of the electronic Gibbs energies in Fig. 7a which for convenience are also included into Fig. 7b and c (dotted curves).

At smaller temperatures and volumes, the bcc volume dependence results in a free energy slightly higher than the one for fcc, thus leading to the fcc stabilization region in Fig. 7a (gray shaded). At higher temperatures and volumes, the bcc electronic free energy "slides" down relatively fast with temperature due to the strong negative volume dependence. This "sliding down" is responsible for the strong curvature of the bcc Gibbs energy and hence also the reason for the bcc stabilization region (green shaded in Fig. 7a). With this, we have therefore identified the origin of the low temperature dependence of the overall Gibbs energy difference in Fig. 6.

It remains, however, to explain why GGA seems to behave qualitatively different, i.e., showing a rather smooth dependence in $\Delta G^{\mathrm{bcc-fcc}}$. For that purpose, Fig. 7b and c contains additionally the projection of $\widetilde{F}^{\mathrm{el}}(T, V)$ for GGA (blue lines). We recognize a similar behavior for the fcc phase as already found for LDA, i.e., only negligible volume dependence. The situation is different for bcc. For GGA, the bcc electronic free energy has only a very small volume dependence which is even opposite to LDA (i.e., increasing with volume and temperature). This clear qualitative difference between LDA and GGA is rather unexpected and we have therefore put further effort in elucidating this matter.

The first attempt is to verify the quality of the PAW potential. While the cross checks for $T=0\,\mathrm{K}$ showed already a good performance of the PAW potential, the small energy differences being relevant here and the new type of free energy contribution might change the picture. In particular, considering the large underestimation of the equilibrium volume by the LDA functional (cf. blue dashed vertical and black dash-dotted vertical line in Fig. 7b or c) thus resulting in an increased internal pressure (higher bulk modulus) might lead to a loss of accuracy of the PAW potential. Such considerations, however, have not been affirmed as the comparison of the PAW free energy with FLAPW results in Fig. 7c (green pluses) clearly demonstrates.

We follow therefore a different route to gain further insight. To explain the approach note first that the relevant volume ranges (at least for moderate pressures) for LDA and GGA do not overlap (i.e., the blue and orange curves in Fig. 7b and c are clearly separated). This means that there is a large mismatch in absolute volumes between the two functionals. If we now extend the region of interest and calculate for each functional the Helmholtz free energy at volumes native to the other functional, we obtain a volume dependence as shown by the open symbols in Fig. 7b and c. For fcc the situation stays the same, i.e., no volume dependence. In contrast for bcc, we find now a very similar volume dependence between LDA and GGA, but only if we consider absolute volumes. We conclude therefore that the seemingly inconsistent behavior between LDA and GGA bcc is a volume effect: At absolute volumes the functionals do behave consistently.

D. Theory vs. Experiment I: Extension of the LDA-GGA similarity to vibronic free energies

Having the full Helmholtz/Gibbs free energy surface as a function of volume/pressure and temperature at hand we can extract any thermodynamic quantity. We will discuss in the following the thermal linear expansion and the linear expansion coefficient [Eq. (4)]. Even though the latter contains almost the same information, it can reveal discrepancies more clearly. We will also discuss the (isothermal) bulk modulus [Eq. (2)] which, being a second derivative, is even more sensitive to the volume/pressure dependence of the free energy surface.

Our results are shown in Fig. 8. We focus first on the fcc phase where sufficient experimental data is avail-
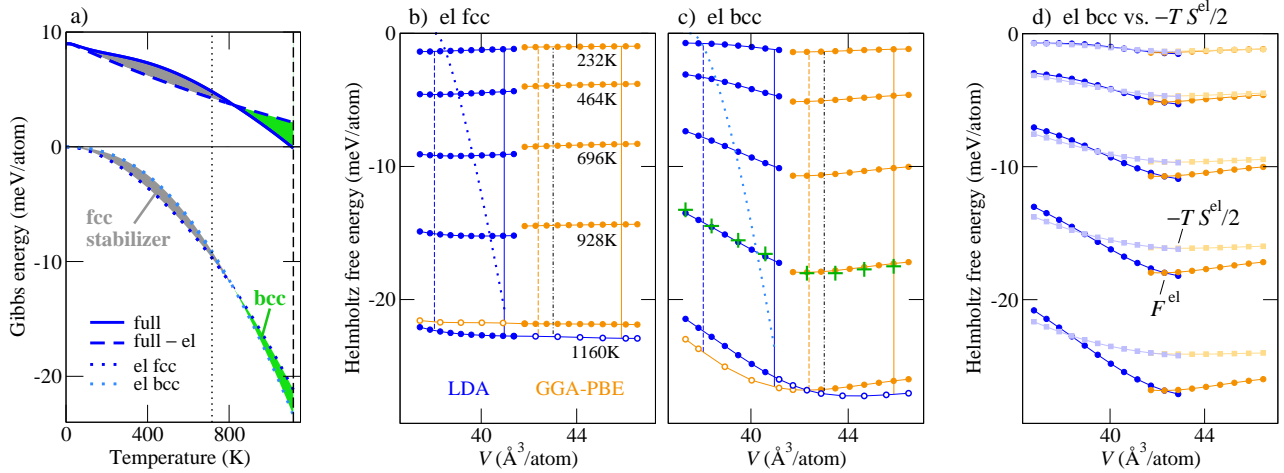
FIG. 7: (Color online) Analysis of the temperature dependence of $\Delta G^{\mathrm{bcc-fcc}}$ for LDA. In a), the solid blue curve reproduces the LDA Gibbs energy difference at P=0.1 GPa from Fig. 6 (full=all excitations included). The dashed curve has all but the electronic excitations included. The dotted curves show the electronic Gibbs energies for each phase separately. The shaded regions indicate whether fcc (gray) or bcc (green) is stabilized by the electronic excitations. In b) and c), the LDA and GGA-PBE electronic Helmholtz free energy is shown as a function of the volume V for fcc and bcc, respectively. For each combination (e.g., LDA fcc), the free energy is plotted for the five given electronic temperatures. The vertical lines indicate the equilibrium volumes at T=0 K (dashed; black dash-dotted=experiment) and at the melting temperature (solid). The curves with open circles show the continuation of the free energy beyond the normal volume range into the regime of the other functional. The blue dotted curves show the temperature dependence of the Gibbs energy (P=0.1 GPa) and correspond therefore to the dotted curves from a). The green pluses indicate FLAPW results (WIEN2K[22]). d) Similar to c) but this time showing the comparison between the full electronic free energy (darker curves) and the ideal electronic entropy term $-TS^{\mathrm{el}}/2$ (light shaded curves). Part d) is discussed in Sec. III B.

able for comparison. We omit, however, the gray marked thermal expansion data from Schulze[49] since they appear to have large error bars as is indicated by their intrinsic scatter and also by the significant deviation from the other measurements. Comparing with the remaining experimental data we find a good agreement with both of the investigated functionals LDA and GGA. In fact, an important observation is that no functional performs better than the other, as opposed to our finding for the fcc phonons where GGA was clearly closer to experiment. For the (fcc) quantities in Fig. 8, we can rather support an interpretation found previously for a larger set of metals:[9] LDA and GGA can be considered as approximate generic upper and lower bounds to experimental data allowing us to construct fully *ab initio* based error bars for the theoretically computed thermodynamic data.

An analysis of such approximate error bars allows then to quickly identify problematic cases.[9] In fact, performing this analysis carefully in the present case reveals a possibly unphysical dependence of the experimental expansion. As mentioned above, the expansion coefficient can magnify discrepancies so let us focus on Fig. 8b. Analyzing the temperature range around 300 K, we notice that the Touloukian data[50] lie slightly higher than both LDA and GGA, i.e., not within the *ab initio* error bars. Considering the full Touloukian curve,[50] we find that what is even more striking is the difference in slopes in the ex-

pansion coefficient. The Touloukian data[50] shows weak temperature dependence above 300 K, while both LDA and GGA have a significantly stronger increase with temperature. Comparing to expansion coefficients for other elements (e.g., Ref. [50] or [52]) it appears that it is rather the experimental data for fcc Ca that is unusual. Other elements show indeed an increasing expansion coefficient with temperature as does also theory predict for fcc Ca.

Turning now to the high temperature bcc phase, we find a scarce experimental situation. No data are available for the bulk modulus and only an older measurement for the thermal expansion from Bernstein.[51] Unfortunately, the authors report difficulties with the measurement and estimate rather large error bars. Therefore, a comparison with our theoretical data would be inconclusive for the quantities shown in Fig. 8. We will come back to this issue when discussing the heat capacity in Sec. IV E. For the moment, let us concentrate on an intrinsic theoretical comparison.

For that purpose, note the following trend in the fcc *ab initio* curves in Fig. 8: When we move from a) to b) and then to c), the difference between the LDA and GGA curves increases. A similar trend occurs also for the bcc phase, it is, however, shadowed in Fig. 8 by the fact that the shown bcc linear expansion and bcc bulk modulus are referenced with respect to T=0 K fcc values. These trends are not merely a technical artefact (e.g., used scale), but are indeed based on a deeper phys-
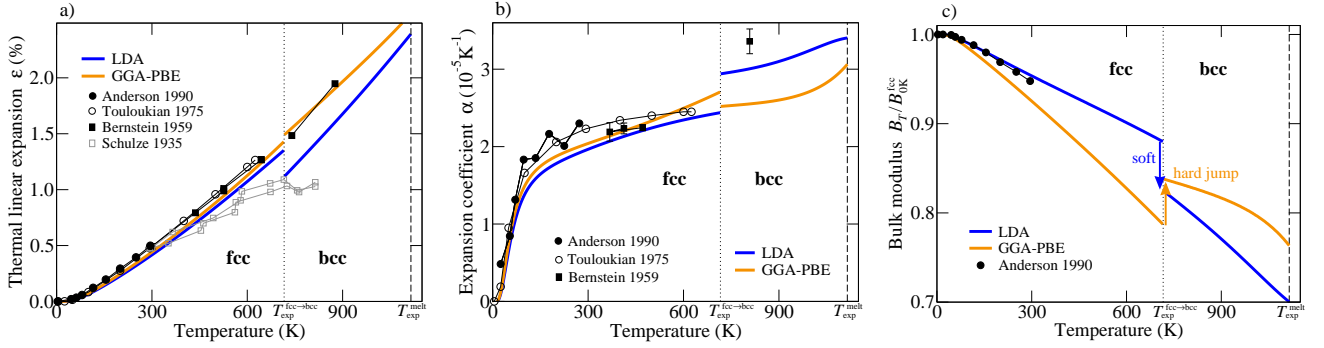
FIG. 8: (Color online) Thermodynamic properties at ambient pressure (0.1 GPa) derived from the free energy surface including all studied excitation mechanisms. The vertical lines indicate the experimental fcc to bcc transition temperature[31] $T_{\mathrm{exp}}^{\mathrm{fcc}\to\mathrm{bcc}} = 716\,\mathrm{K}$ and melting temperature[31] $T_{\mathrm{exp}}^{\mathrm{melt}} = 1115\,\mathrm{K}$. The experimental data are from ● Anderson,[44] ○ Touloukian,[50] ■ Bernstein[51] (including error bars), and □ Schulze.[49] Shown are a) the thermal linear expansion $\epsilon(T)$ [Eq. (4)], b) the linear expansion coefficient $\alpha(T)$ [Eq. (4)], and c) the isothermal bulk modulus $B_T(T)$ [Eq. (2)] relative to its $T=0\,\mathrm{K}$ value in the fcc phase $B_{0\mathrm{K}}^{\mathrm{fcc}}$.

ical argument. The reason is that upon moving from a) to c), the quantities probe more and more sensitively the volume dependence of the Helmholtz free energy surface. Therefore, as mentioned above, the (isothermal) bulk modulus is the most sensitive in this respect. Correlating this argument with the difference between LDA and GGA, we can draw a very important conclusion: A main difference between LDA and GGA in describing thermodynamic quantities originates in their different volume/pressure dependence of the Helmholtz/Gibbs free energy surface.

We can extend this statement even further by a combined analysis of the LDA and GGA results for both of the phases fcc and bcc. To this end, note in Fig. 8c the following behavior: While for the fcc phase the LDA functional yields a harder system (i.e., higher bulk modulus) than GGA, we see a jump at the transition temperature to an exactly opposite picture in the bcc phase. For bcc, GGA yields the harder material with a higher bulk modulus. We label the behavior at the transition temperature a "soft jump" for LDA and a "hard jump" for GGA (Fig. 8c). Concluding, we see that the difference in the free-energy volume dependence (or equivalently Gibbs energy pressure dependence) between LDA and GGA is different for fcc and bcc, i.e., error cancellation does not take place.

This conclusion is rather unfortunate, since it significantly lowers the predictive power of an *ab initio* approach. Based on a detailed analysis, we are however able to remedy this situation.

For the following analysis, we concentrate on the quasiharmonic contribution to the temperature dependence of the bulk modulus which contains a major part of the effect. Further, we need to relate the quasiharmonic bulk modulus to the quasiharmonic free energy surface F^{qh}. It turns out that considering the free energy on an absolute scale brings little insight. The reason is that the strong temperature dependence of F^{qh} hides the relevant volume effects. It is much more revealing to perform
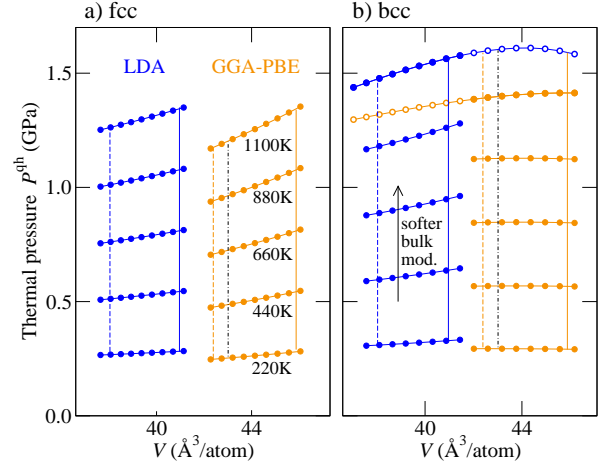

FIG. 9: (Color online) Volume dependence of the quasiharmonic contribution to the thermal pressure P^{qh} at different temperatures for the a) fcc and b) bcc phase. The vertical lines indicate the equilibrium volumes at $T=0\,\mathrm{K}$ (dashed; black dash-dotted=experiment at $T=0\,\mathrm{K}$) and at the melting temperature (solid). The curves with open circles in b) show the continuation of the pressure beyond the normal volume range into the regime of the other functional.

the analysis using instead the derivative of the free energy surface along volume, aka the pressure surface. We therefore construct a two dimensional representation of the quasiharmonic pressure surface $P^{\mathrm{qh}}(V,T)$ shown in Fig. 9. Since Fig. 9 is a rather unconventional representation, let us explain it in a bit more detail.

The quasiharmonic pressure surface constitutes the dominant part of the thermal pressure surface and it is constructed by taking the negative derivative of the quasiharmonic free energy surface with respect to volume. We see only positive pressures for all volumes and temperatures in Fig. 9, because the quasiharmonic con-

tribution (i.e., the non-interacting phonon gas) is purely repulsive. It creates an inner pressure driving the system to larger volumes, i.e., thermal pressure. This effect increases with temperature as can be clearly seen in Fig. 9 (see for instance the orange curves for GGA fcc with the temperatures included). The increase with temperature is eventually the reason for thermal expansion which can be explicitly obtained upon adding the quasi-harmonic pressure to a corresponding $T=0\,\mathrm{K}$ pressure-volume curve. Taking the negative derivative (scaled with volume) of the pressure we arrive directly at the isothermal bulk modulus. Relating this to Fig. 9 means that a steeper positive slope of the pressure curve results in a softer material (i.e., in a lower bulk modulus; see for instance LDA bcc becoming softer with increasing temperature as indicated by the arrow).

With that background we can come back to the analysis of the LDA and GGA bulk modulus for fcc and bcc. The soft and hard jumps of the bulk moduli in Fig. 8c can be understood in terms of the slopes of the pressure curves in Fig. 9. Focus first on LDA and note that P^{qh} has a slightly higher slope at the same temperature for bcc than for fcc. This explains the soft jump of the LDA bulk modulus at the transition temperature in Fig. 8c. In contrast for GGA, we find that P^{qh} in Fig. 9 has a higher slope for fcc. In fact, GGA bcc has almost no slope. This explains the opposite behavior of the GGA bulk modulus resulting in a hard jump at the transition temperature.

Having traced back the effect to the volume dependence of the Helmholtz free energy/pressure surface, we can now perform the next crucial step. Similarly as in the previous section for the electronic free energy, we extend the volume region for each functional beyond its own regime, in order to cover also the volumes native to the other functional (indicated by the open circles in Fig. 9). Looking at the pressure curves in the full volume range allows us to draw an important conclusion which perfectly fits our result for the electronic excitations discussed in the previous section: Both, LDA and GGA follow a similar quasiharmonic free energy curve if compared on an absolute volume scale. However, due to the different placement on this curve which is caused by a differing equilibrium volume at $T=0\,\mathrm{K}$, we see differences in the thermodynamic properties which involve derivatives of the free energy along the volume axis.

Note also that for bcc we can even closely relate the similarity in the quasiharmonic curve with the electronic free energy curve from Fig. 7c. The curvatures are opposite (convex vs concave), but the placement with respect to the minimum on each curve is strikingly similar. For instance, in both cases (quasiharmonic and electronic) the bcc phase lies in the minimum of the general free energy vs. volume curve. In fact, we can complete the discussion by noting that also the anharmonic contribution follows a similar volume dependence as can be seen by a detailed inspection of the trend shown in Fig. 2.

E. Theory vs. Experiment II: Resolution of the disagreement in the experimental heat capacity

The presented methodology is ideally suited to evaluate experimental heat capacities. Accurate heat capacities are a crucial ingredient in constructing phase diagrams, e.g., within the CALPHAD approach, but their experimental determination is – particularly at high temperatures – often accompanied by large scatter in the data. Only very recently *ab initio* has reached a level where it can help evaluating the quality of experimental data.[14,53,54]

The experimental situation in Ca is shown in Fig. 10a. In particular in the bcc phase we observe two strongly disagreeing experimental sets of measurements. In the CALPHAD parametrization only one of the sets is used while the other is disregarded. The data set chosen for the CALPHAD parametrization shows a steep increase with temperature and reaches a relatively high value of more than $5k_{\mathrm{B}}$ at the melting temperature. The other set of experimental data shows a clearly weaker increase with temperature reaching only a value of about $4k_{\mathrm{B}}$ at the melting point.

Our results for the LDA and GGA based heat capacities including all excitation mechanisms are also shown in Fig. 10a. At temperatures < 300 K, the experimental situation is decisive and we see an excellent agreement with theoretical data from both functionals. At higher temperatures, we find that the *ab initio* theory shows an excellent agreement with the lower experimental data. A further important observation is that even at temperatures close to the melting point, LDA and GGA show a very similar qualitative and quantitative behavior for the heat capacity. Following the discussion in Ref. [9], we can consider LDA and GGA as approximate *ab initio* error bars. Thus based on their close agreement we confirm the lower set and rule out the upper one. The presently employed CALPHAD parametrization should therefore be reconsidered.

Fig. 10b decomposes the heat capacity into the respective contributions from various excitations. Clearly, at temperatures above ≈ 300 K the harmonic limit of $3\,k_{\mathrm{B}}$ of non-interacting phonons (at fixed volume) is reached (Dulong-Petit law) being the most important contribution. To describe the linear increase with temperature, we need to include the quasiharmonic as well as the electronic excitations. Both are similar in magnitude contributing together $\approx 1/4$ of the total heat capacity. The anharmonic term describing phonon-phonon interactions, which was of high relevance in explaining the phase transition (see Sec. IV B) is negligible in the heat capacity. It is slightly positive for the fcc phase and negative for bcc, but only roughly $1/50$ of the total heat capacity. In contrast, while being negligible for the phase transition, vacancies are showing a non-negligible contribution in the bcc phase at temperatures close to the melting point. The reason is that despite their small absolute free energy, the exponential decrease in temperature causes a
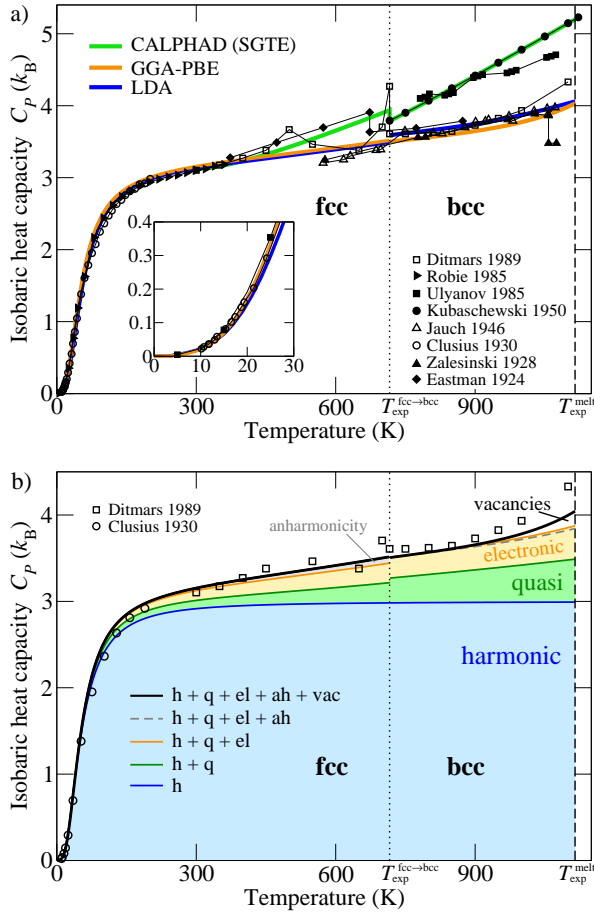
FIG. 10: (Color online) a) Isobaric heat capacity C_P [Eq. (3)] of fcc and bcc Ca at ambient pressure (0.1 GPa) containing all studied excitation mechanisms and b) the influence of the latter for the GGA-PBE functional. The vertical lines indicate the experimental fcc to bcc transition temperature[31] $T_{exp}^{fcc \to bcc} = 716$ K and melting temperature[31] $T_{exp}^{melt} = 1115$ K. CALPHAD data are taken from the SGTE database.[43] Experimental values are from □ Ditmars,[55] ▶ Robie,[56] ■ Ulyanov,[57] ● Kubaschewski,[58] △ Jauch,[59] ○ Clusius,[60] ▲ Zalesinski,[61] ♦ Eastman.[62] See Fig. 6 for further notation.

strong second derivative (aka heat capacity).

A crucial contribution significantly lowering the Gibbs energy of vacancy formation turns out to be anharmonicity. The relatively high value for the enthalpy of formation of 0.84 eV at $T=0$ K (Tab. III) is strongly lowered at the melting temperature by -0.2 eV by anharmonic excitations while quasiharmonic interactions only account for a lowering of -0.07 eV and the electronic influence is of even less importance ($+0.02$ eV).

V. CONCLUSIONS

We have studied all relevant finite temperature excitation mechanisms on the prototype temperature-driven fcc to bcc transition in calcium solely based on *ab initio*

techniques. Extensive convergence checks and methodological advancements allowed us to reach a numerical accuracy of better than 0.5 meV/atom in the standard contributions ($T=0$ K energy, electronic, quasiharmonic, and vacancy excitations) and of below 1 meV/atom in the explicitly anharmonic term. The high numerical accuracy and a detailed analysis of the two currently most popular exchange correlation functionals, LDA and GGA, allowed us to derive systematic and general trends and to elucidate the presently achievable accuracy with density-functional-theory. Key findings are summarized in the following.

Bcc instability. Upon a careful study of the long wave length limit of the $T_1[110]$ branch in the bcc phonon dispersion, we have revealed a dynamical instability at $T=0$ K and ambient pressure. We have shown that the instability significantly depends on the electronic temperature/broadening which can even lead to a full stabilization. The effect is very similar to a pressure-induced stabilization and we can relate both to the behavior of the electronic density of states at the Fermi level. Moreover, we have devised a method to qualitatively evaluate the effect of phonon-phonon interactions on this long wave length instability and have shown that they lead to additional stabilization. Based on this insight we proposed a straightforward method to deal with such instabilities in quasiharmonic and anharmonic calculations.

Phase transition. The key finding is that the temperature dependence of the Gibbs energy difference between bcc and fcc is found to be in very good agreement with experimental (CALPHAD) data. Of crucial importance is the influence of anharmonic excitations shifting the Gibbs energy difference by several meV/atom in favor of fcc. In particular, the temperature dependence is altered significantly by anharmonicity and only upon inclusion of this contribution we find the good agreement with experiment. While the temperature dependence of the Gibbs energy difference is predicted with good accuracy, we find that the actual value at the experimental phase transition temperature is overestimated by ≈ 6 meV/atom for both functionals LDA and GGA. This rather small overestimation leads, however, to a drastic error on the temperature axis of ≈ 400 K. We ascribe this mainly to a failure of the used xc functionals in predicting a correct $T=0$ K energy difference. In this respect, van der Waals interactions, which are missing in LDA and GGA, could play an important role.[63]

Free energy vs. volume curve. Based on a comparison of several derived thermodynamic properties with experiment and on an intrinsic theoretical comparison between LDA and GGA, we have been able to derive the dependence of a general free energy vs. volume curve. This is meant in the sense that both xc functionals follow a very similar Helmholtz free energy curve when taken at the same absolute volume. The difference between the functionals is only due to the different relative placement on that general curve. While LDA is placed at very small absolute volumes due to the well known overbind-

ing, GGA is found at larger volumes in much closer agreement with experiment. The different relative placement on the curve results in strongly varying derivatives along the volume axis. The bulk modulus which probes the volume dependence most sensitively shows therefore the largest differences between LDA and GGA.

Heat capacity. The extensive compilation of experimental data for the heat capacity of calcium reveals a clear distinction between two systematically deviating sets of experiments at high temperatures with intolerable differences of up to $1k_B$. From our numerically highly accurate free energy surface we are able to derive a reliable theoretical prediction of the isobaric heat capacity. Since the studied xc functionals show negligible differences in the heat capacities we can with great confidence assess the quality of the experimental data. A surprising outcome is that for Ca the well established and widely employed CALPHAD SGTE database[43] is *not* based on the best available set of experiments. A reparametrization should be considered.

The multitude of studied properties allows to draw important general conclusions as to which performance one can expect from traditional DFT xc functionals. Let us recap: We find a good agreement with experiment and between LDA and GGA for the temperature dependence of the Gibbs energy difference. The actual value at the phase transition is, however, overestimated by both functionals. We find strong differences in the volume dependence between LDA and GGA resulting, e.g., in a strongly differing bulk modulus. The heat capacity is instead excellently described and the difference between LDA and GGA is insignificant.

In combining these results, a unified picture emerges that shows how differently the various properties probe the Helmholtz free energy surface $F(V,T)$ [or equivalently the Gibbs energy surface $G(P,T)$]. The actual value of the Gibbs energy difference at the phase transition is directly related to the $T=0$ K energy difference between the phases. We do not expect this difference to be in perfect agreement with experiment within a meV scale since its determination involves substantial geometrical differences. The large differences in the volume dependence and related properties of the functionals are due to the discussed different relative placement on a similar absolute free energy curve. In contrast, the temperature dependence of the Gibbs energy difference and the heat capacity are dominated by the temperature dependencies of the free energy surface. From the results of the present study we expect this dependency to be described accurately.

The methodology and insight gained in the present study are an important step towards a fully *ab initio* and numerical approach to compute accurate and reliable input for thermodynamic modelling and to identify the performance but also the limitations of present day xc functionals.

Acknowledgments

[1] A. M. Teweldeberhan, J. L. Dubois, and S. A. Bonev, Phys. Rev. Lett. **105**, 235503 (2010).

[2] P. Söderlind, J. A. Moriarty, and J. M. Wills, Phys. Rev. B **53**, 14063 (1996).

[3] P. Söderlind, Adv. Phys. **47**, 959 (1998).

[4] A. M. Teweldeberhan and S. A. Bonev, Phys. Rev. B **78**, 140101 (2008).

[5] M. A. Uijttewaal, T. Hickel, J. Neugebauer, M. E. Gruner, and P. Entel, Phys. Rev. Lett. **102**, 035702 (2009).

[6] H. Fujihisa, Y. Nakamoto, K. Shimizu, T. Yabuuchi, and Y. Gotoh, Phys. Rev. Lett. **101**, 095503 (2008).

[7] P. Hohenberg and W. Kohn, Phys. Rev. **136**, B864 (1964).

[8] P. A. Varotsos and K. D. Alexopoulos, *Thermodynamics of Point Defects and Their Relation with Bulk Properties*, vol. 14 of *Defects in Solids* (North-Holland, Amsterdam, 1986).

[9] B. Grabowski, T. Hickel, and J. Neugebauer, Phys. Rev. B **76**, 024309 (2007).

[10] N. D. Mermin, Phys. Rev. **137**, A1441 (1965).

[11] D. C. Wallace, *Thermodynamics of Crystals* (Dover, New York, 1998).

[12] S. Biernacki and M. Scheffler, Phys. Rev. Lett. **63**, 290 (1989).

[13] L. Vočadlo and D. Alfè, Phys. Rev. B **65**, 214105 (2002).

[14] B. Grabowski, L. Ismer, T. Hickel, and J. Neugebauer, Phys. Rev. B **79**, 134106 (2009).

[15] A. Moitra, S. G. Kim, and M. F. Horstemeyer, CALPHAD **35**, 262 (2011).

[16] B. Grabowski, T. Hickel, and J. Neugebauer, Phys. Status Solidi B **248**, 1295 (2011).

[17] P. E. Blöchl, Phys. Rev. B **50**, 17953 (1994).

[18] G. Kresse and J. Furthmüller, Phys. Rev. B **54**, 11169 (1996).

[19] G. Kresse and J. Furthmüller, Comput. Mater. Sci. **6**, 15 (1996).

[20] G. Kresse and D. Joubert, Phys. Rev. B **59**, 1758 (1999).

[21] S. Cottenier, *Density Functional Theory and the Family of (L)APW-Methods: A Step-by-Step Introduction* (Instituut voor Kern- en Stralingsfysica, K.U.Leuven, Belgium, 2002), URL http://www.wien2k.at/reg_user/textbooks/.

[22] P. Blaha, K. Schwarz, G. Madsen, D. Kvasnicka, and J. Luitz, *WIEN2k, An Augmented Plane Wave + Local Orbitals Program for Calculating Crystal Properties* (Tech-

nische Universität Wien, Austria, 2001).

[23] J. M. Wills, O. Eriksson, M. Alouani, and D. L. Price, *Full-Potential LMTO Total Energy and Force Calculations*, Electronic Structure and Physical Properties of Solids: The Uses of the LMTO Method (Springer-Verlag, Berlin, 2000).

[24] D. M. Ceperley and B. J. Alder, Phys. Rev. Lett. **45**, 566 (1980).

[25] J. P. Perdew and A. Zunger, Phys. Rev. B **23**, 5048 (1981).

[26] J. P. Perdew, K. Burke, and M. Ernzerhof, Phys. Rev. Lett. **77**, 3865 (1996).

[27] M. Methfessel and A. T. Paxton, Phys. Rev. B **40**, 3616 (1989).

[28] P. Vinet, J. Ferrante, J. H. Rose, and J. R. Smith, J. Geophys. Res. [Solid Earth Planets] **92**, 9319 (1987).

[29] R. E. Cohen, O. Gülseren, and R. J. Hemley, Am. Mineral. **85**, 338 (2000).

[30] R. B. Phillips, *Crystals, defects and microstructures: modeling across scales* (Cambridge University Press, 2001).

[31] C. B. Alcock, M. W. Chase, and V. Itkin, J. Phys. Chem. Ref. Data **22**, 1 (1993).

[32] J. Cao and B. J. Berne, J. Chem. Phys. **99**, 2902 (1993).

[33] M. Born and J. R. Oppenheimer, Ann. Phys. **389**, 457 (1927).

[34] T. Hickel, B. Grabowski, F. Körmann, and J. Neugebauer, J. Phys.: Condens. Matter (2011), in print.

[35] K. Parlinski, Z. Q. Li, and Y. Kawazoe, Phys. Rev. Lett. **78**, 4063 (1997).

[36] G. Kresse, J. Furthmüller, and J. Hafner, Europhys. Lett. **32**, 729 (1995).

[37] D. Alfè, G. D. Price, and M. J. Gillan, Phys. Rev. B **64**, 045123 (2001).

[38] E. R. Davidson, *Methods in Computational Molecular Physics* (Plenum, New York, 1983).

[39] C. Stassis, J. Zaretsky, D. K. Misemer, H. L. Skriver, B. N. Harmon, and R. M. Nicklow, Phys. Rev. B **27**, 3303 (1983).

[40] S. Mukherjee, R. E. Cohen, and O. Gülseren, J. Phys.: Condens. Matter **15**, 855 (2003).

[41] P. Giannozzi, S. Gironcoli, P. Pavone, and S. Baroni, Phys. Rev. B **43**, 7231 (1991).

[42] N. Saunders, A. P. Miodownik, and A. T. Dinsdale, CALPHAD **12**, 351 (1988).

[43] A. T. Dinsdale, CALPHAD **15**, 317 (1991).

[44] M. S. Anderson, C. A. Swenson, and D. T. Peterson, Phys. Rev. B **41**, 3329 (1990), numerical differentiation (central difference) of the given experimental expansion data to obtain the expansion coefficient.

[45] P. W. Bridgman, Proc. Am. Acad. Arts Sci. **58**, 181 (1923), (cited from Ref. [44]).

[46] P. W. Bridgman, Proc. Am. Acad. Arts Sci. **72**, 207 (1938), (cited from Ref. [44]).

[47] S. N. Vaidya and G. C. Kennedy, J. Phys. Chem. Solids **31**, 2329 (1970), (cited from Ref. [44]).

[48] D. E. Gray, ed., *American Institute of Physics (AIP). Handbook* (New York: McGraw-Hill, 1972), (cited from Ref. [44]).

[49] A. Schulze, Phys. Z. **36**, 595 (1935), (cited from Ref. [50]).

[50] Y. S. Touloukian, R. K. Kirby, R. E. Taylor, and P. D. Desai, *Thermal Expansion: Metallic Elements and Alloys*, vol. 12 of *Thermophysical Properties of Matter* (IFI/Plenum, New York, 1975).

[51] B. T. Bernstein and J. F. Smith, Acta Cryst. **12**, 419 (1959), see also Ref. [64].

[52] B. Grabowski, Ph.D. thesis, Universität Paderborn (2009), URL http://dups.ub.uni-paderborn.de/hs/content/titleinfo/1376.

[53] F. Körmann, A. Dick, B. Grabowski, B. Hallstedt, T. Hickel, and J. Neugebauer, Phys. Rev. B **78**, 033102 (2008).

[54] A. Dick, F. Körmann, T. Hickel, and J. Neugebauer, Phys. Rev. B **84**, 125101 (2011).

[55] D. A. Ditmars (1989), (originally unpublished, cited from Ref. [31]).

[56] R. A. Robie (1985), (originally unpublished, cited from Ref. [31]).

[57] S. N. Ulyanov, Ph.D. thesis, Inst. for High Temp., Moscow (1985), (cited from Ref. [31]).

[58] O. Kubaschewski, Z. Metallkd. **41**, 445 (1950).

[59] R. Jauch, Ph.D. thesis, Techn. Hochschule, Stuttgart (1946), (cited from Ref. [31]).

[60] K. Clusius and J. Vaughen, J. Am. Chem. Soc. **52**, 4684 (1930), (cited from Ref. [31]).

[61] E. Zalesinski and R. Zulinski, Bull. Intern. Acad. Polon., Part A **9**, 479 (1928), (cited from Ref. [31]).

[62] E. D. Eastman, A. M. Williams, and T. F. Young, J. Am. Chem. Soc. **46**, 1178 (1924).

[63] J. Klimeš, D. R. Bowler, and A. Michaelides, Phys. Rev. B **83**, 195131 (2011).

[64] We average the experimental linear expansion coefficient given in Ref. [51] over values corresponding to the same temperature interval. The respective temperature is taken as the mean of the given interval. To obtain the thermal linear expansion for fcc (not given in Ref. [51]) a constant expansion coefficient is assumed within the corresponding temperature interval. Additionally, the thermal linear expansion of fcc from Ref. [50] (specifically only the difference between 299 K and 0 K) is used to change the reference to $T = 0$ K. For bcc, the two lattice constants given in Ref. [51] (5.5884 Å for fcc at 299 K and 4.480 Å for bcc at 740 K) and again the thermal linear expansion of fcc from Ref. [50] are first used to calculate the thermal expansion of bcc at 740 K. Then to obtain the bcc value at 876 K we assume that the bcc expansion coefficient for the range 740 K to 876 K given in Ref. [51] is constant. Note that Ref. [50] which cites Ref. [51] contains an inaccuracy ($\approx 33\%$) in the bcc values. The reason is that an assumption of a constant expansion coefficient over a much large temperature interval (room temperature to 740 K) is made. This assumption is, however, unnecessary since additional information in form of the lattice constants is given in Ref. [51] which, as described above and employed in the present study, can be used to retain the desired accuracy in the derived thermal linear expansion.